Ocean spectral data assimilation without background error covariance matrix

Peter C. Chu*, Chenwu Fan, and Tetyana Margolina

Naval Ocean Analysis and Prediction Laboratory, Department of Oceanography

Naval Postgraduate School, Monterey, California, USA

*Corresponding author address: Department of Oceanography, Naval Postgraduate School, Monterey, CA 93943. Email: pcchu@nps.edu

Abstract

Predetermination of background error covariance matrix **B** is challenging in existing ocean data assimilation schemes such as the optimal interpolation (OI). An optimal spectral decomposition (OSD) has been developed to overcome such difficulty without using the **B** matrix. The basis functions are eigenvectors of the horizontal Laplacian operator, pre-calculated on the base of ocean topography, and independent on any observational data and background fields. Minimization of analysis error variance is achieved by optimal selection of the spectral coefficients. Optimal mode truncation is dependent on the observational data and observational error variance and determined using the steep-descending method. Analytical 2D fields of large and small mesoscale eddies with white Gaussian noises inside a domain with 4 rigid and curved boundaries are used to demonstrate the capability of the OSD method. The overall error reduction using the OSD is evident in comparison to the OI scheme. Synoptic monthly gridded world ocean temperature, salinity, and absolute geostrophic velocity datasets produced with the OSD method and quality controlled by the NOAA National Centers for Environmental Information (NCEI) are also presented.

1. Introduction

In ocean data assimilation (or analysis), the coordinates (x, y, z) are usually represented by the position vector $\mathbf{r}$ with grid points represented by $\mathbf{r}_n$, $n = 1, 2, \ldots, N$, and observational locations represented by $\mathbf{r}^{(m)}$, $m = 1, 2, \ldots M$. Here, N is the total number of the grid points, and M is the total number of observational points. A single or multiple variables $\boldsymbol{c} = (u, v, T, S, \ldots)$, no matter two or three dimensional, can be ordered by grid point and by variable, forming a single vector of length NP with N the total number of grid points and P the number of variables. For multiple variables, non-dimensionalization is conducted before forming a single vector $\boldsymbol{c}$ (Chu et al. 2015) with "true", analysis, and background fields ($\mathbf{c}_t$, $\mathbf{c}_a$, $\mathbf{c}_b$) and observational data ($\mathbf{c}_o$) being represented by N and M dimensional vectors,

$$\mathbf{c}_{t,a,b}^T = \left[c_{t,a,b}(\mathbf{r}_1), c_{t,a,b}(\mathbf{r}_2), ..., c_{t,a,b}(\mathbf{r}_N) \right], \quad \mathbf{c}_o^T = \left[c_o(\mathbf{r}^{(1)}), c_o(\mathbf{r}^{(2)}), ..., c_o(\mathbf{r}^{(M)}) \right], \tag{1}$$

where the superscript 'T' means transpose. The innovation (or called the observational increment

$$\mathbf{d} \equiv \left(\mathbf{c}_o - \mathbf{H}\mathbf{c}_b \right), \tag{2}$$

represents the difference between the observational and background data at the observational points $\mathbf{r}^{(m)}$. Here, $\mathbf{H} = [h_{mn}]$ is an $M \times N$ linear observation operator matrix converting the background field $\boldsymbol{c}_b$ (at the grid points, $\mathbf{r}_n$) into "first guess observations" at the observational points $\mathbf{r}^{(m)}$ (Fig. 1).

The analysis error ($\boldsymbol{\varepsilon}_a$) and observational error ($\boldsymbol{\varepsilon}_o$) are defined by

$$\boldsymbol{\varepsilon}_a = \mathbf{c}_a - \mathbf{c}_t, \quad \boldsymbol{\varepsilon}_o \equiv \mathbf{H}^T \mathbf{c}_o - \mathbf{c}_t, \tag{3a}$$

which are evaluated at the **grid points**. The two errors are usually independent of each other,

$$\left\langle \boldsymbol{\varepsilon}_o^T \boldsymbol{\varepsilon}_a \right\rangle = 0, \quad \langle \ \rangle \equiv \frac{1}{N-1} \sum_{n=1}^{N} [\ ]. \tag{3b}$$

Minimization of the analysis error variance

$$E^2 = \left\langle \boldsymbol{\varepsilon}_a^T \boldsymbol{\varepsilon}_a \right\rangle \rightarrow \min \qquad (4)$$

gives the optimal analysis field $\mathbf{c}_a$ for the "true" field $\mathbf{c}_t$.

A common practice in ocean data assimilation (or analysis) is to use a $N \times M$ weight matrix $\mathbf{W}= [w_{nm}]$ to blend $\mathbf{c}_b$ (at the grid points $\mathbf{r}_n$) with innovation $\mathbf{d}$ (at observational points $\mathbf{r}^{(m)}$) (Evensen, 2003; Tang and Kleeman 2004; Chu et al. 2004a, 2015; Galanis et al. 2006; Oke et al. 2008; Han et al. 2013; Yan et al. 2015)

$$\mathbf{c}_a = \mathbf{c}_b + \mathbf{W}\mathbf{d} . \qquad (5)$$

Minimization of the analysis error variance with respect to weights,

$$\partial E^2 / \partial w_{nm} = 0 . \qquad (6)$$

determines the weight matrix

$$\mathbf{W} = \mathbf{B}\mathbf{H}^T (\mathbf{H}\mathbf{B}\mathbf{H}^T + \mathbf{R})^{-1} . \qquad (7)$$

Here, $\mathbf{B}$ is the $N \times N$ background error covariance matrix; $\mathbf{R}$ is the $M \times M$ observational error covariance matrix and is usually simplified as a product of an observational error variance (e_o^2) and an identity matrix $\mathbf{I}$,

$$\mathbf{R} = e_o^2 \mathbf{I} . \qquad (8)$$

Substitution of (7) into (5) leads to the optimal interpolation (OI) equation,

$$\mathbf{c}_a = \mathbf{c}_b + \mathbf{B}\mathbf{H}^T (\mathbf{H}\mathbf{B}\mathbf{H}^T + \mathbf{R})^{-1}\mathbf{d} , \qquad (9)$$

which produces the analysis field $\mathbf{c}_a$ from the innovation $\mathbf{d}$. The challenge for the OI method is the determination of the background error covariance matrix $\mathbf{B}$.

An alternative approach is to use a spectral method with lateral boundary (Γ) information to decompose the variable anomaly at the grid points $[c(\mathbf{r}_n) - c_b(\mathbf{r}_n)]$ into (Chu et al. 2015),

$$c_a(\mathbf{r}_n) - c_b(\mathbf{r}_n) = s_K(\mathbf{r}_n), \quad s_K(\mathbf{r}_n) \equiv \sum_{k=1}^{K} a_k \, \phi_k(\mathbf{r}_n), \tag{10}$$

where $\{\phi_k\}$ are basis functions; K is the mode truncation. The eigenvectors of the Laplace operator with the same lateral boundary condition of $(c - c_b)$ can be used as the set of the basis functions $\{\phi_k\}$ and written in matrix (Chu et al. 2015)

$$\mathbf{\Phi} = \{\phi_{kn}\} = \begin{bmatrix} \phi_1(\mathbf{r}_1) & \phi_2(\mathbf{r}_1) & ... & \phi_K(\mathbf{r}_1) \\ \phi_1(\mathbf{r}_2) & \phi_2(\mathbf{r}_2) & ... & \phi_K(\mathbf{r}_2) \\ ... & ... & ... & ... \\ \phi_1(\mathbf{r}_N) & \phi_2(\mathbf{r}_N) & ... & \phi_K(\mathbf{r}_N) \end{bmatrix}. \tag{11}$$

For a given mode truncation K, minimization of the analysis error variance (4) with respect to the spectral coefficients

$$\partial E_K^2 / \partial a_k = 0, \quad k = 1, ..., K \tag{12}$$

gives the spectral ocean data assimilation equation (Chu et al. 2015),

$$\mathbf{c}_a = \mathbf{c}_b + \mathbf{F}\mathbf{\Phi}^T \left[\mathbf{\Phi}\mathbf{F}\mathbf{\Phi}^T \right]^{-1} \mathbf{\Phi}\mathbf{H}^T \mathbf{d}, \tag{13}$$

where $\mathbf{F}$ is an $N \times N$ (diagonal) observational contribution matrix

$$\mathbf{F} = \begin{bmatrix} f_1 & 0 & 0 & 0 & 0 & 0 \\ 0 & f_2 & 0 & 0 & 0 & 0 \\ 0 & 0 & \ddots & 0 & 0 & 0 \\ 0 & 0 & 0 & f_n & 0 & 0 \\ 0 & 0 & 0 & 0 & \ddots & 0 \\ 0 & 0 & 0 & 0 & 0 & f_N \end{bmatrix}, \quad f_n \equiv \sum_{m=1}^{M} h_{nm}. \tag{14}$$

Here, the matrices $\mathbf{\Phi}$, $\mathbf{F}$, and $\mathbf{H}$ are all given in comparison to the OI equation (9) where the background error covariance matrix $\mathbf{B}$ needs to be determined.

This spectral method has been proven effective for the ocean data analysis. Chu el al. (2003a, b) named the spectral method as the optimal spectral decomposition (OSD). With it, several new ocean phenomena have been identified from observational data such as a bi-modal

structure of chlorophyll-a with winter/spring (February–March) and fall (September–October) blooms in the Black Sea (Chu et al. 2005a), fall–winter recurrence of current reversal from westward to eastward on the Texas–Louisiana continental shelf from the current-meter, near-surface drifting buoy (Chu et. al 2005b), propagation of long Rossby waves at mid-depths (around 1000 m) in the tropical North Atlantic from the Argo float data (Chu et al. 2007), and temporal and spatial variability of the global upper ocean heat content (Chu 2011) from the data of the Global Temperature and Salinity Profile Program (GTSPP, Sun et al. 2009).

The spectral mode truncation is the key for the success of the OSD method. It acts as a spatial low pass filter for the fields to allow the highest wavenumbers corresponding to the highest spectral eigenvalues without aliasing due to the information provided from the observational network.

Questions arise: Can a simple and effective mode truncation method be developed to take into account of model resolution (i.e., total number of model grid points)? What are the major differences between OI and OSD? What is the quality and uncertainty of the OSD method? The purpose of this paper is to answer these questions. The remainder of the paper is organized as follows. Section 2 describes error analysis. Section 3 presents the steep-descending mode truncation method. Section 4 shows idealized "truth" and "observational" fields. Section 5 compares analysis fields between OSD and OI. Section 6 introduces three synoptic monthly gridded world ocean temperature, salinity, and absolute geostrophic velocity datasets produced with the OSD method and quality controlled by the NOAA National Centers for Environmental Information (NCEI). Conclusions are given in Section 7. Appendices A and B briefly describe several methods to determine the H matrix. Appendix C shows the determination of basis

functions. Appendix D presents the Vapnik-Chervonkis dimension for mode truncation. Appendix E depicts a special B matrix for this study.

2. Error Analysis

Low mode truncation does not represent the reality well, while high mode truncation may contain too much noise. Let the truncated spectral representation $\mathbf{s}_K$ in (10) at the grid points form an N-dimensional vector,

$$\mathbf{s}_K^T = \left[s_K(\mathbf{r}_1), s_K(\mathbf{r}_2), ..., s_K(\mathbf{r}_N) \right]. \tag{15}$$

The M-dimensional innovation vector [see (2)]

$$\mathbf{d}^T = \left[d(\mathbf{r}^{(1)}), d(\mathbf{r}^{(2)}), ..., d(\mathbf{r}^{(M)}) \right]$$

at observational points can be transformed into the grid points

$$D_n \equiv D(\mathbf{r}_n) = \frac{\sum_{m=1}^{M} h_{nm} d^{(m)}}{f_n}, \quad f_n \equiv \sum_{m=1}^{M} h_{nm}, \tag{16}$$

where $D(\mathbf{r}_n)$ represents the observational innovation at the grid points,

$$D(\mathbf{r}_n) = c_o(\mathbf{r}_n) - c_b(\mathbf{r}_n). \tag{17}$$

From Eq(3a), observations at grid points are computed using $c_o(\mathbf{r}_n) = \mathbf{H}^T c_o(\mathbf{r}_m)$. The original background state, $c_b(\mathbf{r}_n)$, keeps in the grid space. The matrix form of (16) is

$$\mathbf{FD} = \mathbf{H}^T \mathbf{d}, \tag{18}$$

where f_n denotes contribution of all observational data unto the grid point $\mathbf{r}_n$. The larger the value of f_n, the larger the observational influence on that grid point ($\mathbf{r}_n$). $\mathbf{D}$ is an N-dimensional vector at the grid points,

$$\mathbf{D}^T = (D_1, D_2, ..., D_N) \tag{19}$$

The analysis error (i.e., analysis c_a versus "truth" c_t) in the spectral data assimilation [see (10)] is given by

$$\begin{aligned}\varepsilon_a(\mathbf{r}_n) &\equiv c_a(\mathbf{r}_n) - c_t(\mathbf{r}_n) \\ &= \left[c_a(\mathbf{r}_n) - c_b(\mathbf{r}_n)\right] - \left[c_o(\mathbf{r}_n) - c_b(\mathbf{r}_n)\right] + \left[c_o(\mathbf{r}_n) - c_t(\mathbf{r}_n)\right] \\ &= s_K(\mathbf{r}_n) - D(\mathbf{r}_n) + \varepsilon_o(\mathbf{r}_n)\end{aligned} \tag{20}$$

Here, (10) and (17) are used. The analysis error is decomposed into two parts

$$\varepsilon_a(\mathbf{r}_n) = \varepsilon_K(\mathbf{r}_n) + \varepsilon_o(\mathbf{r}_n), \tag{21}$$

with the truncation error given by

$$\varepsilon_K(\mathbf{r}_n) = s_K(\mathbf{r}_n) - D(\mathbf{r}_n), \tag{22a}$$

and the observational error given by

$$\varepsilon_o(\mathbf{r}_n) = c_o(\mathbf{r}_n) - c_t(\mathbf{r}_n). \tag{22b}$$

3. Steep-Descending Mode Truncation

The Vapnik-Chervonkis dimension (Vapnik 1983; Chu et al. 2003a, 2015) was used to determine the optimal mode truncation K_{opt}. As depicted in Appendix D, it depends only on the ratio of the total number of observational points (M) versus spectral truncation (K) and does not depend on the total number of model grid points (N). This method neglects observational error and ignores the model resolution. In fact, the analysis error variance over the whole domain is given by

$$E_a^2 \equiv \left\langle \left[\boldsymbol{\varepsilon}_a^T \mathbf{F} \boldsymbol{\varepsilon}_a \right] \right\rangle = \left\langle \left[\boldsymbol{\varepsilon}_K^T \mathbf{F} \boldsymbol{\varepsilon}_K \right] \right\rangle + 2 \left\langle \left[\boldsymbol{\varepsilon}_K^T \mathbf{F} \boldsymbol{\varepsilon}_o \right] \right\rangle + \left\langle \left[\boldsymbol{\varepsilon}_o^T \mathbf{F} \boldsymbol{\varepsilon}_o \right] \right\rangle, \quad \left\langle \left[\boldsymbol{\varepsilon}_o^T \mathbf{F} \boldsymbol{\varepsilon}_o \right] \right\rangle = \frac{M}{N} e_o^2, \tag{23}$$

where e_o^2 is the observational error variance [see (8)]. Here, the observational error is assumaed the same at grid points as at the grid points. This is due to the simplification of the error covariance matrix $\mathbf{R} = e_o^2 \mathbf{I}$. The Cauchy-Schwarz inequality shows that

$$E_a^2 \le \left\langle \left[\boldsymbol{\varepsilon}_K^T \mathbf{F} \boldsymbol{\varepsilon}_K \right] \right\rangle + 2\sqrt{\left\langle \left[\boldsymbol{\varepsilon}_K^T \mathbf{F} \boldsymbol{\varepsilon}_K \right] \right\rangle} \sqrt{\left\langle \left[\boldsymbol{\varepsilon}_o^T \mathbf{F} \boldsymbol{\varepsilon}_o \right] \right\rangle} + \left\langle \left[\boldsymbol{\varepsilon}_o^T \mathbf{F} \boldsymbol{\varepsilon}_o \right] \right\rangle$$
$$= E_K^2 + 2E_K \sqrt{M/N} e_o + (M/N) e_o^2 \qquad (24)$$

The relative analysis error reduction at the mode-K can be expressed by the ratio

$$\gamma_K = \ln\left[\frac{E_{K-1}^2 + 2E_{K-1}\sqrt{M/N} e_o + M e_o^2 / N}{E_K^2 + 2E_K \sqrt{M/N} e_o + M e_o^2 / N} \right], \quad K = 2,3,... \qquad (25)$$

Both E_K and E_{K-1} are large for small K (low-mode truncation), which may lead to a small value of γ_K. Both E_K and E_{K-1} are small for large K (high-mode truncation), which also leads to a small value of γ_K. An optimal truncation should be between the low-mode and high-mode truncations with a larger value (over a threshold) of γ_K. This procedure is illustrated as follows. The values (γ_2, γ_2, …, γ_{K_B}) are calculated using (25) from a large K_B (say 250). The mean and standard deviaition of γ can be computed as,

$$\bar{\gamma} = \frac{1}{K_B - 1} \sum_{K=2}^{K_B} \gamma_K, \; s = \sqrt{\frac{1}{K_B - 2} \sum_{K=2}^{K_B} (\gamma_K - \bar{\gamma})^2} \; . \qquad (26)$$

Suppose that the relative error reductions (γ_2, γ_3, …, γ_{K_B}) satisfy the Gaussian distribution. An 100(1 - α)% upper one-sided confidence bound on γ is given by

$$\gamma_{th} = \bar{\gamma} + z_\alpha s \, , \qquad (27)$$

which is used as the threshold for the mode truncation. Here, z is the random variable satisfying the Gaussian distribution with zero mean and standard deviation of 1. If several γ values exceed the threshold, the highest mode

$$K_{OPT} = \max_{\gamma_K \ge \gamma_{th}} (K) \qquad (28)$$

is selected for mode truncation. After the mode truncation K_{OPT} is determined, the spectral coefficnets (a_k, k = 1, 2, …, K_{OPT}) can be calculated, and so as the truncation error variance $E_{K_{OPT}}^2$.

3.3. Multi-Platform Observations

Let observation be conducted by L instruments with different $e_o^{(l)}$ deployed at $\mathbf{r}_l^{(m_l)}$ (m_l = 1, 2, .., M_L; l = 1, 2, …, L). The total number of observations is $M = \sum_{l=1}^{L} M_l$. The M-dimensional observational vector is represented by

$$\mathbf{c}_o^T = \begin{bmatrix} c_o(\mathbf{r}_1^{(1)}), c_o(\mathbf{r}_1^{(2)}), ..., c_o(\mathbf{r}_1^{(M_1)}), c_o(\mathbf{r}_2^{(1)}), c_o(\mathbf{r}_2^{(2)}), ..., c_o(\mathbf{r}_2^{(M_2)}), ..., \\ c_o(\mathbf{r}_L^{(1)}), c_o(\mathbf{r}_L^{(2)}), ..., c_o(\mathbf{r}_L^{(M_L)}) \end{bmatrix} \tag{29}$$

The observational error variance is given by

$$\left\langle \boldsymbol{\varepsilon}_o^T \mathbf{F} \boldsymbol{\varepsilon}_o \right\rangle = M_1[e_o^{(1)}]^2 + M_2[e_o^{(2)}]^2 + ... + M_L[e_o^{(\mathrm{L})}]^2 . \tag{30}$$

The relative error reduction γ_K for mode truncation (25) is replaced by

$$\gamma_K = \ln\left[\frac{E_{K-1}^2 + 2E_{K-1}\sum_{l=1}^{L}\sqrt{M_l / N}\, e_o^{(l)} + \sum_{l=1}^{L} M_l (e_o^{(l)})^2 / N}{E_K^2 + 2E_K \sum_{l=1}^{L}\sqrt{M_l / N}\, e_o^{(l)} + \sum_{l=1}^{L} M_l (e_o^{(l)})^2 / N} \right], \quad K = 2,3,... \tag{31}$$

After the mode truncation is determined, the OSD equation (13) is used to get the analysis field.

4. "Truth", "Background", and "Observational" Fields

Consider an artificial non-dimensional horizontal domain (-19 < x < 19, -15 < y < 15) with the four curved rigid boundaries (Fig. 2):

$$\begin{aligned} &\frac{x}{10} - 0.3\cos\left(\frac{y}{8}\right)\sin\left(\frac{x}{10}\right) = \xi = \begin{cases} -\pi/2 & \text{(west)} \\ \pi/2 & \text{(east)} \end{cases} \\ &\frac{y}{8} - 0.2\sin\left(\frac{x}{5}\right)\left[1 - \cos\left(\frac{y}{8}\right)\right] = \eta = \begin{cases} -\pi/2 & \text{(south)} \\ \pi/2 & \text{(north)} \end{cases} \end{aligned} \tag{32}$$

The domain is discretized with Δx = Δy = 0.5. The total number of the grid points inside the domain (N) is 3569. Fig. 3 shows the first 12 basis functions $\{\phi_k\}$, which are the eigenvectors of the Laplacian operator with the Dirichlet boundary condition, i.e., b_1 = 0 in (C3) of Appendix C.

The first basis-function $\phi_1(\mathbf{x}_n)$ shows a one-gyre structure. The second and third basis functions $\phi_2(\mathbf{x}_n)$ and $\phi_3(\mathbf{x}_n)$ show the east-west and north-south dual-eddies. The fourth basis-function $\phi_4(\mathbf{x}_n)$ shows the east-west slanted dipole-pattern with opposite signs in the northeastern region (positive) and the southwestern region (negative). The fourth basis-function $\phi_4(\mathbf{x}_n)$ shows the tripole-pattern with negative values in the western and eastern regions and positive values in between. The higher order basis functions have more complicated variability structures.

Two "truth" fields for the non-dimensional domain with 4 rigid and curved boundaries (Fig. 2) contain multiple mesoscale eddies (treated as "truth") given by

$$\begin{cases} c_t(x,y) = 25 - y^2/40 + 3\cos\left[L_x\xi(x,y)\right]\sin\left[L_y\eta(x,y)+\beta\right] \\ \xi = \dfrac{x}{10} - 0.3\cos\left(\dfrac{y}{8}\right)\sin\left(\dfrac{x}{10}\right), \quad \eta = \dfrac{y}{8} - 0.2\sin\left(\dfrac{x}{5}\right)\left[1-\cos\left(\dfrac{y}{8}\right)\right], \\ \left(L_x, L_y, \beta\right) = \left(3, 2, \pi/2\right) \end{cases} \tag{33}$$

for the large-eddy field (Fig 4a) and given by

$$\begin{cases} c_t(x,y) = 25 - y^2/40 + 3\cos\left[L_x\xi(x,y)\right]\cos\left[L_y\eta(x,y)+\beta\right] \\ \xi = \dfrac{x}{10} - 0.3\cos\left(\dfrac{y}{8}\right)\sin\left(\dfrac{x}{10}\right), \quad \eta = \dfrac{y}{8} - 0.2\sin\left(\dfrac{x}{5}\right)\left[1-\cos\left(\dfrac{y}{8}\right)\right] \\ \left(L_x, L_y, \beta\right) = \left(7, 5, 0\right) \end{cases} \tag{34}$$

for the small-eddy field (Fig. 4b). The background field is given by

$$c_b(x,y) = 25 - y^2/40 \tag{35}$$

The "observational" points $\{\mathbf{r}^{(m)}\}$ are randomly selected inside the domain (Fig. 5) with the total number (M) of 300. The "observational" points $\{\mathbf{r}^{(m)}\}$ are kept the same for all the sensitivity studies. The domain is discretized by $\Delta x = \Delta y = 0.5$ with total number (N) of grid points of 3,569.

Sixteen sets of "observations" (c_o) are constructed from Figs.4a, b using the analytical values plus white Gaussian noises (ε_o) of zero mean and various standard deviations (σ) from 0 (no noise) to 2.0 with 0.1 increment from 0 to 1.0 and 0.2 increment from 1.0 to 2.0 (total 16 sets), generated by the MATLAB,

$$c_o(\mathbf{r}^{(m)}) = c_t(\mathbf{r}^{(m)}) + \varepsilon_o(\mathbf{r}^{(m)}). \tag{36}$$

Figs. 6a and 6b show 6 out of the 16 constructed sets with σ = (0, 0.2, 0.5, 10., 1.6, 2.0). Both OSD and OI methods are used to get the analysis field $c_a(\mathbf{r}_n)$ from these "observations". The bilinear interpolation (see Appendix B) is used for the observation operator **H** in this study.

5. Comparison between OSD and OI

a. OSD Analysis Fields

The steep-descending mode truncation K_{OPT} depends on the user-input parameter e_o [see (25)] and observational noise σ. E_a^2 and γ_K are computed from the "observational" data in Figs. 6a and 6b. The threshold of mode truncation (27) varies with the significance level α. In this study, (e_0, σ) vary between 0 and 2; α has two levels of (0.05, 0.10) with $z_{0.05}$ = 1.645, $z_{0.10}$ = 1.287 in (27). For given values of e_0 (= 0.2) and σ (= 0.8), the optimal mode truncation depends on the significance level α with K_{OPT} = 58 for α = 0.05 (Fig. 7a) and K_{OPT} = 67 for α = 0.10 (Fig. 7b). Most results shown in this section is for α = 0.05 since it it a commonly used significance level.

For the large-eddy field, K_{OPT} is not sensitive to the values of σ and e_o. It is 7 in the upper-left portion and 6 in the lower-right portion of Table 1. For the small-eddy field, K_{OPT} takes (58, 67) for the most cases, 178 for the high noise levels ($\sigma \geq 1.8$) and low e_o values ($e_o \leq 1.0$), and 82 for the low noise levels ($\sigma \leq 0.1$) and low e_o values ($e_o \leq 0.3$) (Table 2).

The analysis field using the OSD data assimilation (13) for a particular user-input parameter e_o and noise level σ, $c_a^{OSD}(\mathbf{r}_n, e_o, \sigma)$, is represented in Fig. 8a (the large-eddy field) using "observations" in Fig. 6a (with various σ), and in Fig. 8b (the small-eddy field) using "observations" in Fig. 6b (with various σ). Comparison between Figs. 8a, b and Figs. 4a,b demonstrates the capability of the OSD method with the analysis fields $c_a^{OSD}(\mathbf{r}_n, \sigma, e_o)$ fully reconstructed for all occasions.

b. OI Analysis Fields

With the assumption that the c field is statistically stationary and homogeneous, the OI equation (9) with the **R** and **B** matrices represented by (8) and (E1) [see Appendix E] is used to analyze the "observational" data with three user-defined paramters: (r_a, r_b, e_o). Here, r_a and r_b are the decorrelation scale and zero crossing ($r_b > r_a$); e_o is the standard deviation of the observational error. Let these paramters take discrete values with total number of P_a for r_a, P_b for r_b, and P_e for e_o. In this study, we set $P_a = P_b = P_e = 5$. e_o has 5 values (0.2, 0.5, 1.0, 1.5, 2.0). Considering the horizontal domain from -15 to 15 in both (x, y) directions, r_a takes 5 values (2, 3, 4, 5, 6); (r_b - r_a) takes 5 values (0.5, 1.0, 1.5, 2.0, 2.5). There are 125 combinations of (r_a, r_b, e_o) for the test.

The analysis field from the OI data assimilation (9), $c_a^{OI}(\mathbf{r}_n, \sigma, r_a, r_b, e_o)$, with four different sets of user-input parameters (r_a, r_b - r_a, e_o): (2, 2.5, 1), (4, 5.5, 1), (6, 8.5, 1), and (6, 8.5, 2), are presented in Fig. 9a (the large-eddy field) using "observations" in Fig. 6a, and in Fig. 9b (the small-eddy field) using "observations" in Fig. 6b. Comparison between Figs. 9a, b and Figs. 4a,b demonstrates strong dependence of the OI output on the selection of the parameters (r_a, r_b, e_o). For the large-scale eddies (Fig. 9a), the analysis fields c_a are very different from the "truth" field c_t for $r_a = 2$, $r_b = 2.5$, $e_o = 1$ for all "observations" (Fig. 6a); the difference between the

reconstructed and "truth" fields decreases as r_a and r_b increase; the two fields are quite similar when $r_a = 6$, $r_b = 8.5$ for both $e_o = 1$ and 2. Such similarity reduces with increasing e_o. For the small-scale eddies (Fig. 9b), the analysis fields c_a are totally different from the "truth" field c_t for $r_a = 6$, $r_b = 8.5$, $e_o = 1$ and 2 for all "observations" (Fig. 6b), less different as r_a and r_b decrease; and are quite similar to c_t when $r_a = 2$, $r_b = 2.5$, $e_o = 1$.

c. Root Mean Square Error

The analysis field from OSD, c_a^{OSD}, depends only on the observational error variance e_o^2 and its uncertainty is represented by the root mean square error R^{OSD},

$$R^{OSD}(\sigma, e_o) = \sqrt{\frac{1}{N}\sum_{n=1}^{N}\left[c_a^{OSD}(\mathbf{r}_n, \sigma, e_o) - c_t(\mathbf{r}_n)\right]^2}\,. \tag{37a}$$

Average over all the values of e_o leads to the overall uncertainty

$$\bar{R}^{OSD}(\sigma) = \sqrt{\frac{1}{NP_e}\sum_{e_o}\sum_{n=1}^{N}\left[c_a^{OSD}(\mathbf{r}_n, \sigma, e_o) - c_t(\mathbf{r}_n)\right]^2}\,. \tag{37b}$$

The analysis field using OI (c_a^{OI}) depends on three user-defined parameters (r_a, r_b, e_o). Its uncertainty due to a particular parameter is represented by

$$R^{OI}(\sigma, r_a) = \sqrt{\frac{1}{NP_bP_e}\sum_{r_b}\sum_{e_o}\sum_{n=1}^{N}\left[\psi_a^{OI}(\mathbf{r}_n, \sigma, r_a, r_b, e_o) - \psi_t(\mathbf{r}_n)\right]^2}\,, \tag{38a}$$

$$R^{OI}(\sigma, r_b) = \sqrt{\frac{1}{NP_aP_e}\sum_{r_a}\sum_{e_o}\sum_{n=1}^{N}\left[\psi_a^{OI}(\mathbf{r}_n, \sigma, r_a, r_b, e_o) - \psi_t(\mathbf{r}_n)\right]^2}\,, \tag{38b}$$

$$R^{OI}(\sigma, e_o) = \sqrt{\frac{1}{NP_aP_b}\sum_{r_a}\sum_{r_b}\sum_{n=1}^{N}\left[\psi_a^{OI}(\mathbf{r}_n, \sigma, r_a, r_b, e_o) - \psi_t(\mathbf{r}_n)\right]^2}\,, \tag{38c}$$

which are compared to $\bar{R}^{OSD}(\sigma)$ and $R^{OSD}(\sigma, e_o)$.

Fig. 10 shows the comparison between $R^{OI}(\sigma, r_a)$ and $\bar{R}^{OSD}(\sigma)$ for 5 different r_a values: (2, 3, 4, 5, 6) and two types (the large-scale and small-scale) of the "observational" field. $R^{OI}(\sigma, r_a)$ monotonically increases with σ and is generally larger than $\bar{R}^{OSD}(\sigma)$. For the "observations" representing the large-scale eddy fields (L_x = 2, L_y = 3, see Fig. 6a), $\bar{R}^{OSD}(\sigma)$ increases slightly from 0.32 for σ = 0 to 0.34 for σ = 2.0. However, $R^{OI}(\sigma, r_a = 2)$ is always larger than $\bar{R}^{OSD}(\sigma)$ and increases from 0.37 for σ = 0 to 1.13 for σ = 2.0; $R^{OI}(\sigma, r_a \geq 3)$ is smaller than $\bar{R}^{OSD}(\sigma)$ for small σ, equals $\bar{R}^{OSD}(\sigma)$ at certain σ_0, and larger than $\bar{R}^{OSD}(\sigma)$ for $\sigma > \sigma_0$. The value of σ_0 increases with r_a from 0.4 for r_a = 3 to 1.0 for r_a = 6. $R^{OI}(\sigma, r_a = 6)$ increases from 0.13 for σ = 0 to 0.62 for σ = 2.0. For the "observations" representing the small-scale eddy field (L_x = 5, L_y = 7, see Fig. 6b), $\bar{R}^{OSD}(\sigma)$ increases slightly from 0.22 for σ = 0 to 0.27 for σ = 0.4; evidently from 0.27 for σ = 0.4 to 0.40 for σ = 0.5; and slowly from 0.40 for σ = 0.5 to 0.71 for σ = 2.0. However, $R^{OI}(\sigma, r_a)$ is much larger than $\bar{R}^{OSD}(\sigma)$ for any r_a. For example, $R^{OI}(\sigma, r_a = 2)$ increases from 0.43 for σ = 0 to 1.14 for σ = 2.0; …, $R^{OI}(\sigma, r_a = 6)$ increases from 0.89 for σ = 0 to 1.06 for σ = 2.0.

Fig. 11 shows the comparison between $R^{OI}(\sigma, r_b)$ and $\bar{R}^{OSD}(\sigma)$ for 5 different ($r_b - r_a$) values: (0.5, 1.0, 1.5, 2.0, 2.5) and two types (large-scale and small-scale) of the "observational" fields. $R^{OI}(\sigma, r_b)$ monotonically increases with σ and is generally larger than $\bar{R}^{OSD}(\sigma)$. For the "observations" representing the large-scale eddy fields (L_x = 2, L_y = 3, see Fig. 6a), $R^{OI}(\sigma, r_b - r_a)$ monotonically increases with σ from around 0.2 for σ = 0 to around 0.78 for σ = 2.0 for all the values of ($r_b - r_a$) with σ_0 from 0.4 for ($r_b - r_a$) = 0.5 to 0.6 for ($r_b - r_a$) = 2.5. For the "observations" representing the small-scale eddy fields (L_x = 5, L_y = 7, see Fig. 6b),

$R^{OI}(\sigma, r_b - r_a)$ is much larger than $\bar{R}^{OSD}(\sigma)$ for any (r_b -r_a) and σ. For example, $R^{OI}(\sigma, r_b - r_a = 0.5)$ increases from 0.53 for σ = 0 to 1.00 for σ = 2.0; …, $R^{OI}(\sigma, r_b - r_a = 2.5)$ increases from 0.58 for σ = 0 to 1.00 for σ = 2.0.

Fig. 12 shows the comparison between $R^{OI}(\sigma, e_o)$ and $R^{OSD}(\sigma, e_o)$ for 5 different e_o values: (0.2, 0.5, 1.0, 1.5, 2.0) and two types (large-scale and small-scale) of the "observational" fields. First, $R^{OI}(\sigma, e_o)$ monotonically increases with σ and is evidently larger than $R^{OSD}(\sigma, e_o)$ for all σ and e_o. Second, dependence of $R^{OSD}(\sigma, e_o)$ on σ is insensitive to the change of e_o. For the "observations" representing the large-scale eddy fields (L_x = 2, L_y = 3, see Fig. 6a), $R^{OI}(\sigma, e_o)$ is close to $R^{OSD}(\sigma, e_o)$ for σ < 1.2, and much larger than $R^{OSD}(\sigma, e_o)$ for σ > 1.2 with e_o = 0.2 and 0.5; and vice versa with e_o = 1.0, 1.5, and 2.0. $R^{OI}(\sigma, e_o = 2.0)$ increases slightly from 0.98 at σ = 0 to 1.08 at σ = 2.0 and is almost twice of $R^{OSD}(\sigma, e_o)$ for all σ. For the "observations" representing the small-scale eddy fields (L_x = 5, L_y = 7, see Fig. 6b), $R^{OI}(\sigma, e_o)$ is also larger than $R^{OSD}(\sigma, e_o)$. For example, $R^{OI}(\sigma, e_o = 2.0)$ increases slightly from 1.37 at σ = 0 to 1.42 at σ = 2.0, which is 2-3 times of $R^{OSD}(\sigma, e_o = 2.0)$ for σ < 1.0.

The overall performance between OI and OSD with various noise levels (σ) can be estimated by the error ratio,

$$\kappa(\sigma) = \frac{\bar{R}^{OSD}(\sigma)}{\hat{R}^{OI}(\sigma)}, \quad \hat{R}^{OI}(\sigma) \equiv \sqrt{\frac{1}{NP_aP_bP_e}\sum_{r_a}\sum_{r_b}\sum_{e_o}\sum_{n=1}^{N}\left[c_a^{OI}(\mathbf{r}_n, \sigma, r_a, r_b, e_o) - c_t(\mathbf{r}_n)\right]^2}. \quad (39)$$

Fig. 13 shows the dependence of κ(σ) (evidently less than 1) on σ for the two types (large-scale and small-scale eddies) of the "observational" fields represented by Figs 6a and 6b with two different significance levels (α = 0.05, 0.10) for the threshold of mode truncation in the OSD

method (27). At α = 0.05 (Fig. 13a), for the large-scale eddy field, $\kappa(\sigma)$ takes 0.71 at σ = 0; fluctuates with σ; and decreases to 0.57 at σ = 2.0. For the small-scale eddy field, $\kappa(\sigma)$ increases monotonically with σ from 0.43 at σ = 0 to 0.67 at σ = 2.0. At α = 0.10 (Fig. 13b), for the large-scale eddy field, $\kappa(\sigma)$ takes 1.17 at σ = 0; decreases monotonically with σ to 0.40 at σ = 2.0. For the small-scale eddy field, $\kappa(\sigma)$ increases monotonically with σ from 0.36 at σ = 0 to 0.70 at σ = 2.0. It means that the OSD performs better for the test case. Integration of $\kappa(\sigma)$ over the whole interval of the noise level [0, 2.0] yields

$$\hat{\kappa} = \frac{1}{2}\int_0^2 \kappa(\sigma)d\sigma = \begin{cases} \alpha = 0.05 & \alpha = 0.1 & \\ 0.76 & 0.72 & \text{large-scale eddy} \\ 0.51 & 0.59 & \text{small-scale eddy} \end{cases} \tag{40}$$

which means that the overall error for the OSD is 76% (51%) of the OI error for the large-scale (small-scale) eddy field for α = 0.05. The overall performance of the OSD method is relatively insensitive to the selection of the significance level α.

The computational cost of the OSD and OI methods is comparable in the test cases. In the OSD method, the steep-descending method for mode truncation requires (a) the computation of a large number K_b in Eq(26) of eigenvectors, (b) the construction and solution of the OSD equation (13) can be done once for all. In the OI method, however, the construction and solution of the OI equation (9) must be repeated each time background/observations changes.

6. Synoptic Monthly Gridded Temperature and Salinity Fields

The OSD method is used to to produce the synoptic monthly gridded (SMG) temperature (T) and salinity (S) datasets (Chu and Fan 2016a, Chu et al. 2016) from the two world ocean observational (T, S) profile datasets [the NOAA national Centers for Environmental Information (NCEI) ‘s World Ocean Database (WOD) and the Global Temperature and Salinity Profile Program (GTSPP)]. The synoptic monthly gridded absolute geostrophic velocity dataset (Chu

and Fan 2016b) is also established from the SMG-WOD (*T*, *S*) fields using the P vector method (Chu 1995, Chu and Wang 2003). These datasets have been quality controlled by the NCEI professionals and are openly downloaded for public use at http://data.nodc.noaa.gov/geoportal/rest/find/document?searchText=synoptic+monthly+gridded&f=searchPage. The duration is January 1945 to December 2014 for the synoptic monthly gridded WOD (*T*, *S*) and absolute geostrophic velocity fields and January 1990 to December 2009 for the synoptic monthly gridded GTSPP (*T*, *S*) fields.

7. Conclusions

Ocean spectral data assimilation has been developed on the base of the classic theory of the generalized Fourier series expansion such that any ocean field can be represented by a linear combination of the products of basis functions (or called modes) and corresponding spectral coefficients. The basis functions are the eigenvectors of the Laplace operator, determined only by the topography with the same lateral boundary condition for the assimilated variable anomaly. They are pre-calculated and independent on any observational data and background fields. The mode truncation K depends on the observational data and a user input parameter e_o^2 (i.e., observational error variance); and is determined via the steep-descending method.

The OSD completely changes the common ocean data assimilation procedures such as OI, KF, and variational methods, where the background error covariance matrix **B** needs to be pre-determined since the weight matrix **W** is used. However, the OSD uses the spectral form to represent the observational innovation at the grid points [see (17)]. Minimization of the truncation error variance leads to the optimal selection of the spectral coefficients. Thus, the background error covariance matrix **B** vanishes in the OSD procedure since the weight matrix

W is not used. It is contrast to the existing OI method, where the **B** matrix is often assumed to be stationary and homogeneous with user-defined parameters.

The capability of the OSD method is demonstrated through its comparison to OI using analytical 2D fields of large and small mesoscale eddies inside a domain with 4 rigid and curved boundaries as "truth", and addition to the "truth" of white Gaussian noises with zero mean and standard deviations (σ) varying from 0 (no noise) to 2.0 with 0.1 increment at randomly selected locations used as "observations." A simple covariance function (Bretherton, 1976) was used for the OI procedure with three user-defined parameters (r_a, r_b, e_o) taking 5 possible values each. The OSD uses the same value of e_o. The performance of OSD and OI is compared by (1) patterns for each set of 125 combinations of parameters, (2) root mean square errors for varying parameters, and (3) overall root mean square erros. The results show that the overall error reduction using the OSD is evident, which is 76% (51%) [72% (59%)] for significance level α = 0.05 (α = 0.10) of the OI error for the large-scale (small-scale) eddy field. In context of practical application, synoptic monthly gridded world ocean temperature, salinity, and absolute geostrophic velocity datasets have been produced with the OSD method and quality controlled by the NOAA National Centers for Environmental Information (NCEI).

Two issues need to be addressed on the correlation matrix. First, the comparison between the OSD and OI is at one particular instant in time. The **B** matrix used in the OI is based only on distance. Second, in the covariance-matrix based methods, when the covariance matrix is fixed once and for all, it is well-known that the very first data assimilation cycle is doing well, but subsequent cycles are less effective because the remaining error has a tendency to be orthogonal to the directions of the covariance matrix. In the OSD method, the correction is based on spectral functions (i.e. basis functions) chosen once-and-for all. More sophisticated, flow-based

covariance matrix will allow OI to perform much better. Further verification and validation under real-time ocean conditions are needed to verify the quality of OSD in time cycles and to compare between OSD and OI methods.

In the two test cases (large and small eddy fields), it is clear that the optimal mode truncation K_{OPT} (around 6 for the large eddy field and around 60 for the small eddy field) are very closed to the number of eigenvectors required to represent the truth field (Fig. 4). This shows the capability of the steep-descending mode truncation. However, the performance of the method for the truth field is a mixture of large and small scales in different parts of the domains needs to be further investigated.

Acknowledgments. The Office of Naval Research, the Naval Oceanographic Office, and the Naval Postgraduate School supported this study.

Appendix A. Determination of H-Matrix Using All Grid Points

IDW interpolation, using all grid points, is one of the most commonly used techniques for interpolation based on the assumption that the value of h_{mn} in H-matrix are influenced more by the nearby points and less by the more distant points. Let

$$d_n^m = \sqrt{(x^{(m)} - x_i)^2 + (y^{(m)} - y_j)^2} \qquad \text{(A1)}$$

be the distance between the grid point (x_i, y_j) and observational point $(x^{(m)}, y^{(m)})$. The influence of the grid point $\mathbf{x}_n$ on the observational point $\mathbf{x}^{(m)}$ is given by (Spepard 1968)

$$h_{mn} = \left(d_n^m\right)^{-q} / \sum_{n=1}^{N} \left(d_n^m\right)^{-q} \qquad \text{(A2)}$$

where q is an arbitrary positive real number called the power parameter (typically, $q = 2$). Another form of h_{mn} is given by (Franke and Nielson 1991)

$$h_{mn} = \frac{[(D^{(m)} - d_n^m)/D^{(m)} d_n^m]^2}{\sum_{n=1}^{N}[(D^{(m)} - d_n^m)/D^{(m)} d_n^m]^2}, \qquad \text{(A3)}$$

where $D^{(m)}$ is the distance from the observational point $\mathbf{x}^{(m)}$ to the most distant grid point. Eq.(A3) has been found to give better results than (A2) . As a result, $c_b(\mathbf{x}^{(m)}, t)$, is somewhat symmetric about each grid point.

Appendix B. Determination of H-Matrix Using Neighboring Grid Points

Consider the position vector $\mathbf{x} = (x, y)$ located inside the grid cell (Fig. B-1),

$$x_i \le x < x_{i+1},\ y_j \le y < y_{j+1}.$$

Mathematically, the variable c_b at $\mathbf{r}$ (inside the grid cell) can be represented approximately by a polynomial,

$$c_b(\mathbf{r}) = \sum_{\alpha=0}^{L}\sum_{\beta=0}^{L} A_{\alpha\beta}(x - x_i)^{\alpha}(y - y_j)^{\beta} \qquad \text{(B1)}$$

where $L = 1$ refers to the bilinear interpolation, and $L = 3$ leads to the bicubic interpolation. For the bilinear interpolation, Eq.(B1) becomes

$$c_b(\mathbf{r}) = A_{00} + A_{10}(x - x_i) + A_{01}(y - y_j) + A_{11}(x - x_i)(y - y_j) \qquad \text{(B2)}$$

or in matrix notation,

$$c_b(\mathbf{r}) = \begin{bmatrix} 1 & (x - x_i) \end{bmatrix} \begin{bmatrix} A_{00} & A_{01} \\ A_{10} & A_{11} \end{bmatrix} \begin{bmatrix} 1 \\ (y - y_j) \end{bmatrix}. \qquad \text{(B3)}$$

Since c_b at four neighboring grid points: $c_b(x_i, y_j)$, $c_b(x_{i+1}, y_j)$, $c_b(x_{i+1}, y_j)$, $c_b(x_{i+1}, y_{j+1})$ are given, substitution of the four values into (B2) leads to the determination of the four coefficients A_{00}, A_{10}, A_{01}, A_{11}. Using these coefficients, the bilinear interpolation (B2) becomes

$$c_b(\mathbf{r}) = \frac{c_b(x_{i+1}, y_{j+1})}{(x_{i+1}-x_i)(y_{j+1}-y_j)}(x-x_i)(y-y_j) + \frac{c_b(x_{i+1}, y_j)}{(x_{i+1}-x_i)(y_{j+1}-y_j)}(x-x_i)(y_{j+1}-y)$$
$$+ \frac{c_b(x_i, y_{j+1})}{(x_{i+1}-x_i)(y_{j+1}-y_j)}(x_{i+1}-x)(y-y_j) + \frac{c_b(x_i, y_j)}{(x_{i+1}-x_i)(y_{j+1}-y_j)}(x_{i+1}-x)(y_{j+1}-y) \quad \text{(B4)}$$

Let the observational point $\mathbf{r}^{(m)}$ be located in the grid cell,

$$x_i \le x^{(m)} < x_{i+1},\ y_j \le y^{(m)} < y_{j+1}.$$

Evaluation of c_b at the observational point $\mathbf{r}^{(m)}$ using (B3) leads to

$$c_b(\mathbf{r}^{(m)}) = p_{i,j}^{(m)} c_b(x_i, y_j) + p_{i+1,j}^{(m)} c_b(x_{i+1}, y_j) + p_{i,j+1}^{(m)} c_b(x_i, y_{j+1}) + p_{i+1,j+1}^{(m)} c_b(x_{i+1}, y_{j+1}) \quad \text{(B5)}$$

where the proportional coefficients $\{ p_{i,j}^{(m)}, p_{i+1,j}^{(m)}, p_{i,j+1}^{(m)}, p_{i+1,j+1}^{(m)} \}$ are defined by

$$p_{i,j}^{(m)} = \frac{(x_{i+1}-x^{(m)})(y_{j+1}-y^{(m)})}{(x_{i+1}-x_i)(y_{j+1}-y_j)}, \quad p_{i+1,j}^{(m)} = \frac{(x^{(m)}-x_i)(y_{j+1}-y^{(m)})}{(x_{i+1}-x_i)(y_{j+1}-y_j)},$$

$$p_{i,j+1}^{(m)} = \frac{(x_{i+1}-x^{(m)})(y^{(m)}-y_j)}{(x_{i+1}-x_i)(y_{j+1}-y_j)} \quad p_{i+1,j+1}^{(m)} = \frac{(x^{(m)}-x_i)(y^{(m)}-y_j)}{(x_{i+1}-x_i)(y_{j+1}-y_j)}. \quad \text{(B6)}$$

It is noted that the proportionality coefficients $\{ p_{i,j}^{(m)}, p_{i+1,j}^{(m)}, p_{i,j+1}^{(m)}, p_{i+1,j+1}^{(m)} \}$ depend solely on the location of the observational points ($\mathbf{r}^{(m)}$), and

$$p_{i,j}^{(m)} + p_{i+1,j}^{(m)} + p_{i,j+1}^{(m)} + p_{i+1,j+1}^{(m)} = 1. \quad \text{(B7)}$$

Setting L =3 in (B1) leads to the bicubic spline interpolation,

$$c_b(\mathbf{r}) = A_{00} + A_{10}(x-x_i) + A_{01}(y-y_j) + A_{11}(x-x_i)(y-y_j)$$
$$+ A_{20}(x-x_i)^2 + A_{02}(y-y_j)^2 + A_{30}(x-x_i)^3 \quad \text{(B8)}$$
$$+ A_{21}(x-x_i)^2(y-y_j) + A_{12}(x-x_i)(y-y_j)^2 + A_{03}(y-y_j)^3$$

or in matrix notation,

$$c_b(\mathbf{r}) = \begin{bmatrix} 1 & (x-x_i) & (x-x_i)^2 & (x-x_i)^3 \end{bmatrix} \begin{bmatrix} A_{00} & A_{01} & A_{02} & A_{03} \\ A_{10} & A_{11} & A_{12} & 0 \\ A_{20} & A_{21} & 0 & 0 \\ A_{30} & 0 & 0 & 0 \end{bmatrix} \begin{bmatrix} 1 \\ (y-y_j) \\ (y-y_j)^2 \\ (y-y_j)^3 \end{bmatrix} \quad \text{(B9)}$$

which is rewritten by

$$c_b(\mathbf{r}) = \begin{bmatrix} 1 & x & x^2 & x^3 \end{bmatrix} \begin{bmatrix} 1 & -x_i & x_i^2 & -x_i^3 \\ 0 & 1 & -2x_i & 3x_i^2 \\ 0 & 0 & 1 & -3x_i \\ 0 & 0 & 0 & 1 \end{bmatrix}$$
$$\begin{bmatrix} A_{00} & A_{01} & A_{02} & A_{03} \\ A_{10} & A_{11} & A_{12} & 0 \\ A_{20} & A_{21} & 0 & 0 \\ A_{30} & 0 & 0 & 0 \end{bmatrix} \begin{bmatrix} 1 & 0 & 0 & 0 \\ -y_j & 1 & 0 & 0 \\ y_j^2 & -2y_j & 1 & 0 \\ -y_j^3 & 3y_j^2 & 3y_j & 1 \end{bmatrix} \begin{bmatrix} 1 \\ y \\ y^2 \\ y^3 \end{bmatrix} \quad \text{(B10)}$$

Determination of the ten coefficients (A_{00}, A_{01}, A_{02}, A_{03}, A_{10}, A_{11}, A_{12}, A_{20}, A_{21}, A_{30}) requires not only the values,

$$A_{00} = c_b(x_i, y_j),$$

$$A_{00} + A_{10}\Delta x + A_{20}(\Delta x)^2 + A_{30}(\Delta x)^3 = c_b(x_{i+1}, y_j),$$

$$A_{00} + A_{01}\Delta y + A_{02}(\Delta y)^2 + A_{03}(\Delta y)^3 = c_b(x_i, y_{j+1}),$$

$$\begin{aligned} &A_{00} + A_{10}\Delta x + A_{01}\Delta y + A_{11}\Delta x\Delta y + A_{20}(\Delta x)^2 + A_{02}(\Delta y)^2 \\ &+A_{30}(\Delta x)^3 + A_{21}(\Delta x)^2\Delta y + A_{12}\Delta x(\Delta y)^2 + A_{03}(\Delta y)^3 \\ &= c_b(x_{i+1}, y_{j+1}), \end{aligned} \quad \text{(B11)}$$

but also the derivatives at the neighboring grid points

$$A_{10} = \partial c_b(x_i, y_j)/\partial x = [c_b(x_{i+1}, y_j) - c_b(x_{i-1}, y_j)]/2\Delta x,$$

$$A_{01} = \partial c_b(x_i, y_j)/\partial y = [c_b(x_i, y_{j+1}) - c_b(x_i, y_{j-1})]/2\Delta y,$$

$$\begin{aligned} &A_{10} + 2(\Delta x)A_{20} + 3(\Delta x)^2 A_{30} = \partial c_b(x_{i+1}, y_j)/\partial x \\ &= [c_b(x_{i+2}, y_j) - c_b(x_i, y_j)]/2\Delta x, \end{aligned}$$

$$A_{10} + (\Delta y)A_{11} + (\Delta y)^2 A_{12} = \partial c_b(x_i, y_{j+1}) / \partial x$$
$$= [c_b(x_{i+1}, y_{j+1}) - c_b(x_{i-1}, y_{j+1})] / 2\Delta x,$$

$$A_{01} + (\Delta x)A_{11} + (\Delta x)^2 A_{21} = \partial c_b(x_{i+1}, y_j) / \partial y$$
$$= [c_b(x_{i+1}, y_{j+1}) - c_b(x_{i+1}, y_{j-1})] / 2\Delta y,$$

$$A_{01} + 2(\Delta y)A_{01} + 3(\Delta y)^2 A_{03} = \partial c_b(x_i, y_{j+1}) / \partial y$$
$$= [c_b(x_i, y_{j+2}) - c_b(x_i, y_j)] / 2\Delta y. \quad \text{(B12)}$$

The solution of the above set of 10 linear algebraic equations (B11) and (B12) leads to the determination of the ten coefficients (A_{00}, A_{01}, A_{02}, A_{03}, A_{10}, A_{11}, A_{12}, A_{20}, A_{21}, A_{30}). It is noted that values of c_b at the 10 neighboring grid points (x_i, y_j), (x_{i+1}, y_j), (x_i, y_{j+1}), (x_{i+1}, y_{j+1}), (x_{i-1}, y_j), (x_i, y_{j-1}), (x_{i+2}, y_j), (x_{i-1}, y_{j+1}), (x_{i+1}, y_{j-1}), (x_i, y_{j+2}) are used to solve (B11) and (B12). Following (B10), interpolation of c_b at the 10 neighboring grid points on the observational $\mathbf{r}^{(m)}$ [=($x^{(m)}$, $y^{(m)}$] using the bi-cubic interpolation is given by

$$c_b(\mathbf{r}^{(m)}) = \begin{bmatrix} 1 & x^{(m)} & (x^{(m)})^2 & (x^{(m)})^3 \end{bmatrix} \begin{bmatrix} 1 & -x_i & x_i^2 & -x_i^3 \\ 0 & 1 & -2x_i & 3x_i^2 \\ 0 & 0 & 1 & -3x_i \\ 0 & 0 & 0 & 1 \end{bmatrix}$$
$$\begin{bmatrix} A_{00} & A_{01} & A_{02} & A_{03} \\ A_{10} & A_{11} & A_{12} & 0 \\ A_{20} & A_{21} & 0 & 0 \\ A_{30} & 0 & 0 & 0 \end{bmatrix} \begin{bmatrix} 1 & 0 & 0 & 0 \\ -y_j & 1 & 0 & 0 \\ y_j^2 & -2y_j & 1 & 0 \\ -y_j^3 & 3y_j^2 & 3y_j & 1 \end{bmatrix} \begin{bmatrix} 1 \\ y^{(m)} \\ (y^{(m)})^2 \\ (y^{(m)})^3 \end{bmatrix} \quad \text{(B13)}$$

Thus, an equation similar to (B5) can be written for evaluating c_b at the observational point $\mathbf{r}^{(m)}$ with the known 10 coefficients (A_{00}, A_{01}, A_{02}, A_{03}, A_{10}, A_{11}, A_{12}, A_{20}, A_{21}, A_{30},

$$c_b(\mathbf{r}^{(m)}) = p_{i,j}^{(m)} c_b(x_i, y_j) + p_{i+1,j}^{(m)} c_b(x_{i+1}, y_j) + p_{i,j+1}^{(m)} c_b(x_i, y_{j+1})$$
$$+ p_{i+1,j+1}^{(m)} c_b(x_{i+1}, y_{j+1}) + p_{i-1,j}^{(m)} c_b(x_{i-1}, y_j) + p_{i,j-1}^{(m)} c_b(x_i, y_{j-1}) + p_{i+2,j}^{(m)} c_b(x_{i+2}, y_j) \quad \text{(B14)}$$
$$+ p_{i-1,j+1}^{(m)} c_b(x_{i-1}, y_{j+1}) + p_{i+1,j-1}^{(m)} c_b(x_{i+1}, y_{j-1}) + p_{i,j+2}^{(m)} c_b(x_i, y_{j+2})$$

where the 10 corresponding coefficients $\{ p_{i,j}^{(m)}, p_{i+1,j}^{(m)}, p_{i,j+1}^{(m)}, p_{i+1,j+1}^{(m)}, p_{i-1,j}^{(m)}, p_{i,j-1}^{(m)}, p_{i,+2j}^{(m)}, p_{i-1,j+1}^{(m)}, p_{i+1,j-1}^{(m)}, p_{i,j+2}^{(m)} \}$ are analytically determined and depends solely on the location of the observational points ($\mathbf{r}^{(m)}$), and

$$p_{i,j}^{(m)} + p_{i+1,j}^{(m)} + p_{i,j+1}^{(m)} + p_{i+1,j+1}^{(m)} + p_{i-1,j}^{(m)} + p_{i,j-1}^{(m)} + p_{i,+2j}^{(m)} + p_{i-1,j+1}^{(m)} + p_{i+1,j-1}^{(m)} + p_{i,j+2}^{(m)} = 1 \qquad \text{(B15)}$$

Since only 10 neighboring grid points are used to interpolate at the observational point $\mathbf{r}^{(m)}$ using the bicubic interpolation, the matrix **H** has only 10 non-zero values in each row. However, it is too tedious to write it out.

Appendix C. Basis Functions

As pointed by Chu et al. (2015), three necessary conditions should be satisfied in selection of basis-functions $\{ \phi_k(\mathbf{r}) \}$: (i) ***satisfaction of the same homogeneous boundary condition*** of the assimilated variable anomaly, (ii) orthonormality, and (iii) independence on the assimilated variables. The first necessary condition requires the same boundary condition for $(c - c_b)$ and the basis functions $\{ \phi_k \}$. The second necessary condition is given by

$$\iint_{\Gamma} \phi_k(\mathbf{r}) \phi_{k'}(\mathbf{r}) d\mathbf{r} = \delta_{kk'}, \qquad \text{(C1)}$$

where $\delta_{kk'}$ is the Kronecker delta,

$$\delta_{kk'} = \begin{cases} 0 & \text{if } k \neq k' \\ 1 & \text{if } k = k' \end{cases}. \qquad \text{(C2)}$$

Due to their independence on the assimilated variable (the third necessary condition), the basis-functions are available prior to the data assimilation.

The basis functions are the eigenvectors $\{ \phi_k \}$ of the Laplacian operator with the same boundary condition as the variable anomaly $(c - c_b)$,

$$\nabla^2\phi_k = -\lambda_k\phi_k, \quad [b_1(\tau)\mathbf{e}\bullet\nabla\phi_k + b_2(\tau)\phi_k]|_\Gamma = 0, \quad k = 1,...,\infty. \tag{C3}$$

Here, $\{\lambda_k\}$ are the eigenvalues, **e** is the unit vector normal to the boundary; τ denotes a moving point along the boundary, and $[\,b_1(\tau),\ b_2(\tau)\,]$ are parameters varying with τ. The boundary condition in (C3) becomes the Dirichlet boundary condition when $b_1 = 0$, and the Neumann boundary conditions when $b_2 = 0$. As pointed by Chu et al. (2015), different variable anomalies have different $[\,b_1(\tau),\ b_2(\tau)\,]$. For example, the temperature, salinity, and velocity potential anomalies have $b_2 = 0$ for the rigid boundary and $b_1 = 0$ for the open boundary. However, the anomaly has $b_1 = 0$ for the rigid boundary and $b_2 = 0$ for the open boundary. It is obvious that the eigenvectors $\{\phi_k\}$ are orthonormal and independent of the assimilated variables.

Appendix D. Vapnik-Chervonenkis Dimension for Mode Truncation

The Vapnik-Chervonenkis dimension (Vapnik 1983; Chu et al. 2003a, 2015) is to seek the optimal mode truncation on the base of the first term of the analysis error (23),

$$J_{tr} = \left\langle \left[\boldsymbol{\varepsilon}_K^T \mathbf{F} \boldsymbol{\varepsilon}_K \right] \right\rangle = \frac{\sum_{n=1}^{N} [\, f_n (D_n - D_n^{(K)})]^2}{N-1} \tag{D1}$$

with the cost function

$$\begin{aligned} &J_K = J_{tr} + \mu(K, M, \alpha), \\ &\mu(K, M, \alpha) = J_* \sqrt{\frac{[\ln(2M/K)+1] - \ln(\alpha/M)}{M/K}}, \quad K = 1, 2, ..., \infty \end{aligned} \tag{D2}$$

Here, α ($\ll 1$) is the significance level. J_* is the upper bound of J_{tr}. For a given M, J_{tr} decreases monotonically with K; μ increases with K if α is given. The optimal mode truncation is through the minimization of the cost function,

$$\min_K (J_K) = J_{K_{opt}}. \tag{D3}$$

This method neglects observational error [only first term of (23) considered] and ignores the model resolution (represented by the total number of grid points N). The ratio of observational points (M) and the spectral truncation (K) is the key to determine the optimal mode truncation K_{opt}.

Appendix E. B-Matrix

The **B** matrix is often established based on the assumption of statistical stationarity and homogeneity of the reconstructed field with a simple covariance function, for example Bretherton et al. (1976) proposed

$$\mathbf{B} = \left[b_{ij} \right]_{N \times N}, \quad b_{ij} = \left(1 - \frac{r_{ij}^2}{r_b^2} \right) \exp\left(-\frac{r_{ij}^2}{r_a^2} \right), \quad r_{ij}^2 = \left| \mathbf{r}_i - \mathbf{r}_j \right|^2, \quad r_b > r_a, \qquad \text{(E1)}$$

depending on distances only. Here, r_{ij} is the distance between the two grid points $\mathbf{r}_i$ and $\mathbf{r}_{aj}$; r_{ay} and r_b are the decorrelation scale and zero crossing. To conduct the OI data assimilation, the three parameters (e_o, r_a, r_b) need to be defined by user. Chu et al. (1997, 2002) compute auto-correlation functions from historical observational data to fit the Gaussian function and get de-correlation scales for the **B** matrix. Recent studies show that some variables such as upper ocean current speed does not satisfy the normal distribution, but the Weibull distribution (Chu 2008, 2009).

References

Bretherton FP, Davis RE, Fandry CB (1976) A technique for objective analysis and design of oceanographic experiments applied to MODE-73. Deep-Sea Res. Oceanogr. Abstr., 23, 559–582, doi:10.1016/0011-7471(76)90001-2.

Chu (1995) P-vector method for determining absolute velocity from hydrographic data

Chu PC (2008) Probability distribution function of the upper equatorial Pacific current speeds. Geophys Res Lett, 35, doi: 10.1029/2008GL033669.

Chu PC (2009) Statistical characteristics of the global surface current speeds obtained from satellite altimeter and scatterometer data. IEEE J Sel Topics Earth Obs Remote Sensing, 2 (1) 27-32.

Chu PC (2011) Global upper ocean heat content and climate variability. Ocean Dyn, 61 (8), 1189-1204.

Chu PC, Wells SK, Haeger SD, Szczechowski C, Carron M (1997) Temporal and spatial scales of the Yellow Sea thermal variability. J Geophys Res (Oceans), 102, 5655-5668.

Chu PC, Wang GH, Chen YC (2002) Japan/East Sea (JES) circulation and thermohaline structure, Part 3, Autocorrelation Functions. J Phys Oceanogr, 32, 3596-3615.

Chu PC, Wang GH (2003) Seasonal variability of thermohaline front in the central South China Sea. J Oceanogr, 59, 65-78.

Chu PC, Ivanov LM, Korzhova TP, Margolina TM, Melnichenko OM (2003a, b) Analysis of sparse and noisy ocean current data using flow decomposition. Part 1: theory. J Atmos Oceanic Technol, 20, 478–491; Part 2: application to Eulerian and Lagrangian data. J Atmos Oceanic Technol, 20, 492–512.

Chu PC, Wang GH Fan CW (2004a) Evaluation of the U.S. Navy's Modular Ocean Data Assimilation System (MODAS) using the South China Sea Monsoon Experiment (SCSMEX) data. J Oceanogr, 60, 1007-1021.

Chu PC, Ivanov LM, Margolina TM (2004b) Rotation method for reconstructing process and field from imperfect data. Int J Bifur Chaos, 14, 2991–2997.

Chu PC, Ivanov LM, Melnichenko OM (2005a) Fall-winter current reversals on the Texas-Louisiana continental shelf. J Phys. Oceanogr., 35, 902–910.

Chu PC, Ivanov LM, Margolina TM (2005b) Seasonal variability of the Black Sea Chlorophyll-a concentration. J Mar Syst, 56, 243–261.

Chu PC, Ivanov LM, Melnichenko OV, Wells NC (2007) Long baroclinic Rossby waves in the tropical North Atlantic observed from profiling floats. J Geophys Res, 112, C05032, doi:10.1029/2006JC003698.

Chu PC, Tokmakian RT, Fan CW, Sun LC (2015) Optimal spectral decomposition (OSD) for ocean data assimilation. J Atmos Oceanic Technol, 32, 828-841.

Chu PC, Fan CW (2016a) Synoptic monthly gridded three dimensional (3D) World Ocean Database temperature and salinity from January 1945 to December 2014 (NCEI Accession 0140938). NOAA National Centers for Environmental Information (NCEI), http://data.nodc.noaa.gov/cgi-bin/iso?id=gov.noaa.nodc:0140938.

Chu PC, Fan CW (2016b) Synoptic Monthly Gridded WOD Absolute Geostrophic Velocity (SMG-WOD-V) (January 1945 - December 2014) with the P-Vector Method (NCEI Accession 0146195). NOAA National Centers for Environmental Information (NCEI), http://data.nodc.noaa.gov/cgi-bin/iso?id=gov.noaa.nodc:0146195

Chu PC, Fan CW, Sun LC (2016) Synoptic monthly gridded Global Temperature and Salinity Profile Programme (GTSPP) water temperature and salinity from January 1990 to December 2009 (NCEI Accession 0138647). NOAA National Centers for Environmental Information (NCEI), http://data.nodc.noaa.gov/cgi-bin/iso?id=gov.noaa.nodc:0138647.

Cohn SE (1997) Estimation theory for data assimilation problems: Basic concenptual framework and some open questions. J Meteor Soc Japan, 75, 257-288.

Evensen G (2003) The ensemble Kalman filter: theoretical formulation and practical implementation. Ocean Dyn, 53, 343-367.

Franke R, Nielson G (1991) Scattered data interpolation and application: a tutorial and survey. In Hagen H., Roller D. (eds) Geometric modelling, methods and applications. Berlin, Springer, 131-160.

Galanis GN, Louka P, Katsafados Kallos PG, Pytharoulis I (2006) Applications of Kalman filters based on non-linear functions to numerical weather predictions. Ann Geophys, 24, 2451-2460.

Han GJ, Wu XR, Zhang SQ, Liu ZY, Li W (2013) Error covariance estimation for coupled data assimilation using a Lorenz atmosphere and a simple pynocline ocean model. J Climate, 26, 10218-10231.

Ide K, Courtier P, Ghil M (1997) Unified notation for data assimilation: Operational, sequential and variational. J Meteor Soc Japan, 75, 181-189.

Oke PR, Brassington GB, Griffin DA, Schiller A (2008) The Bluelink ocean data assimilation system (BODAS). Ocean Modelling, 21, 46-70.

Spepard D (1968) A two-dimensional interpolation function for irregularly spaced data. Proc 23rd Nat Conf ACM, 517-523.

Sun LC, Thresher A, Keeley R, et al. (2009) The data management system for the Global Temperature and Salinity Profile Program (GTSPP). In Proceedings of the "OceanObs'09: Sustained Ocean Observations and Information for Society" Conference (Vol. 2), Venice, Italy, 21–25 September 2009, Hall, J, Harrison D.E. and Stammer, D., Eds., ESA Publication WPP-306.

Tang Y, Kleeman R (2004) SST assimilation experiments in a tropical Pacific ocean model. *J. Phys. Oceanogr.*, **34**, 623-642.

Vapnik, VH (1983) Reconstruction of Empirical Laws from Observations (in Russian). Nauka, 447 pp.

Yan CX. Zhu J, Xie JP (2015) An ocean data assimilation system in the Indian Ocean and west Pacific Ocean. Adv Atmos Sci, doi: 10.1007/s00376-015-4121-z.

Table 1. Dependence of K_{OPT} on (σ, e_o) for the large-eddy field shown in Fig. 6a with significance level $\alpha = 0.05$.

σ \ e_o	0	0.1	0.2	0.3	0.4	0.5	0.6	0.7	0.8	0.9	1.0	1.2	1.4	1.6	1.8	2.0
0	7	7	7	7	7	7	7	7	7	7	7	7	7	7	7	7
0.1	7	7	7	7	7	7	7	7	7	7	7	7	7	7	7	7
0.2	7	7	7	7	7	7	7	7	7	7	7	7	7	7	7	7
0.3	7	7	7	7	7	7	7	7	7	7	7	7	7	7	7	7
0.4	7	7	7	7	7	7	7	7	7	7	7	7	7	7	7	6
0.5	7	7	7	7	7	7	7	7	7	7	7	7	7	7	6	6
0.6	7	7	7	7	7	7	7	7	7	7	7	7	7	6	6	6
0.7	7	7	7	7	7	7	7	7	7	7	7	7	7	6	6	6
0.8	7	7	7	7	7	7	7	7	7	7	7	7	6	6	6	6
0.9	7	7	7	7	7	7	7	7	7	7	7	6	6	6	6	6
1.0	7	7	7	7	7	7	7	7	7	6	6	6	6	6	6	6
1.2	7	7	6	6	6	6	6	6	6	6	6	6	6	6	6	6
1.4	6	6	6	6	6	6	6	6	6	6	6	6	6	6	6	6
1.6	6	6	6	6	6	6	6	6	6	6	6	6	6	6	6	6
1.8	6	6	6	6	6	6	6	6	6	6	6	6	6	6	6	6
2.0	6	6	6	6	6	6	6	6	6	6	6	6	6	6	6	6

Table 2. Dependence of K_{OPT} on (σ, e_o) for the small-eddy field shown in Fig. 6b with significance level $\alpha = 0.05$.

σ \ e_o	0	0.1	0.2	0.3	0.4	0.5	0.6	0.7	0.8	0.9	1.0	1.2	1.4	1.6	1.8	2.0
0	82	82	82	82	67	67	67	67	67	67	58	58	58	58	58	58
0.1	82	82	82	67	67	67	67	67	67	58	58	58	58	58	58	58
0.2	67	67	67	67	67	67	67	67	67	58	58	58	58	58	58	58
0.3	67	67	67	67	67	67	67	67	58	58	58	58	58	58	58	58
0.4	67	67	67	67	67	67	67	58	58	58	58	58	58	58	58	58
0.5	67	67	67	67	67	67	58	58	58	58	58	58	58	58	58	58
0.6	67	67	67	67	67	58	58	58	58	58	58	58	58	58	58	58
0.7	67	67	67	58	58	58	58	58	58	58	58	58	58	58	58	58
0.8	58	58	58	58	58	58	58	58	58	58	58	58	58	58	58	58
0.9	58	58	58	58	58	58	58	58	58	58	58	58	58	58	58	58
1.0	58	58	58	58	58	58	58	58	58	58	58	58	58	58	58	58
1.2	58	58	58	58	58	58	58	58	58	58	58	58	58	58	58	58
1.4	58	58	58	58	58	58	58	58	58	58	58	58	58	58	58	58
1.6	58	58	58	58	58	58	58	58	58	58	58	58	58	58	58	58
1.8	178	178	178	178	178	178	58	58	58	58	58	58	58	58	58	58
2.0	178	178	178	178	178	178	178	178	178	178	178	58	58	58	58	58

Figure Captions

Fig. 1. Illustration of ocean data assimilation with $\boldsymbol{c}_b$ located at the grid points, and $\boldsymbol{c}_o$ located at the points '*'. The ocean data assimilation is to convert the innovation, $\mathbf{d} = \boldsymbol{c}_o - \mathbf{H}\boldsymbol{c}_b$, from the observational points to the grid points.

Fig. 2. Horizontal non-dimensional domain with four curved rigid boundaries with each boundary given by Eq. (32).

Fig. 3. Basis functions from ϕ_1 to ϕ_{12} for the domain depicted by Eq.(32).

Fig. 4. "Truth" field c_t taken as (a) the analytical function (33) with large-scale eddy field L_x=3, L_y = 2, $\beta = \pi/2$, and (b) the analytical function (34) with small-scale eddy field L_x = 7, L_y = 5, β = 0.

Fig. 5. Randomly selected locations (total: 300) inside the domain as "observational" points.

Fig. 6a. "Observational" data (c_o) from Fig. 4a with added white Gaussian noises of zero mean and various standard deviations: (a) 0 (i.e., no noise) (b) 0.2, (c) 0.5, (d) 1.0, (e) 1.6, and (f) 2.0.

Fig. 6b. "Observational" data (c_o) from Fig. 4b with added white Gaussian noises of zero mean and various standard deviations: (a) 0 (i.e., no noise) (b) 0.2, (c) 0.5, (d) 1.0, (e) 1.6, and (f) 2.0.

Fig. 7. Dependence of E_a^2 and γ_K on K for the "observational" data for the small-scale eddy field with $\sigma = 0.8$ and $e_o = 0.2$ at two significant levels of (a) $\alpha = 0.05$ ($z_{0.05} = 1.645$) and (b) $\alpha = 0.10$ ($z_{0.10} = 1.291$) as the threshold of mode truncation [see Eq.(27)]. The optimal mode truncation is 58 for $\alpha = 0.05$ and 67 for $\alpha = 0.10$.

Fig. 8a. The analysis field c_a obtained by the spectral data assimilation [see Eq.(13)] using the steep-descending mode truncation with the significance level of $\alpha = 0.05$ from the "observations" shown in Fig. 6a with 6 noise (σ) levels (0, 0.2, 0.5, 1.0, 1.6, 2.0) and 4 values of e_o: (a) 0.2, (i.e., no noise), (b) 0.5, (c) 1.0, and (d) 2.0.

Fig. 8b. The analysis field c_a obtained by the spectral data assimilation [see Eq.(13)] using the steep-descending mode truncation with the significance level of $\alpha = 0.05$ from the "observations" shown in Fig. 6b with 6 noise (σ) levels (0, 0.2, 0.5, 1.0, 1.6, 2.0) and 4 values of e_o: (a) 0.2, (i.e., no noise), (b) 0.5, (c) 1.0, and (d) 2.0.

Fig. 9a. The analysis field c_a obtained by the OI data assimilation [see Eq.(9)] for "observations" shown in Fig. 6a various noise levels with various combinations of user-defined parameters (r_a, r_b, e_o,): (2, 2.5, 1), (4, 5.5, 1), (6, 8.5, 1), and (6, 8.5, 2).

Fig. 9b. The analysis field c_a obtained by the OI data assimilation [see Eq.(9)] for "observations" shown in Fig. 6b various noise levels with various combinations of user-defined parameters (r_a, r_b, e_o,): (2, 2.5, 1), (4, 5.5, 1), (6, 8.5, 1), and (6, 8.5, 2).

Fig. 10. Comparison between $R^{OI}(\sigma, r_a)$ and $\bar{R}^{OSD}(\sigma)$ of the analysis fields from the same "observations" with different noise levels with varying parameter r_a = (2, 3, 4, 5, 6) from top to bottom with the left panels using "observations" shown in Fig. 6a and the right panels using "observations" in Fig. 6b. The solid curves represent the OSD with the significance level of α = 0.05; and the dotted curves refer to the OI.

Fig. 11. Comparison between $R^{OI}(\sigma, r_b)$ and $\bar{R}^{OSD}(\sigma)$ of the analysis fields from the same "observations" with different noise levels with different $(r_b - r_a)$ = (0.5, 1.0, 1.5, 2.0, 2.5) with the left panels using "observations" shown in Fig. 6a and the right panels using "observations" in Fig. 6b. The solid curves represent the OSD with the significance level of α = 0.05; and the dotted curves refer to the OI.

Fig. 12. Comparison between $R^{OI}(\sigma, e_o)$ and $R^{OSD}(\sigma, e_o)$ of the analysis fields from the same "observations" with different noise levels with varying parameter e_o = (0.2, 0.5, 1.0, 1.5, 2.0) from top to bottom with the left panels using "observations" shown in Fig. 6a and the right panels using "observations" in Fig. 6b. The solid curves represent the OSD with the significance level of α = 0.05; and the dotted curves refer to the OI.

Fig. 13. Dependence of the error ratio κ [see Eq.(39)] on σ using "observations" in Fig. 6a (represented by dots) and in Fig. 6b (represented by *) with two different significance levels: (a) $\alpha = 0.05$, and (b) $\alpha = 0.10$.

Fig. B1. Interpolation at an observational point $\mathbf{r}^{(m)}$ from four neighboring grid points.

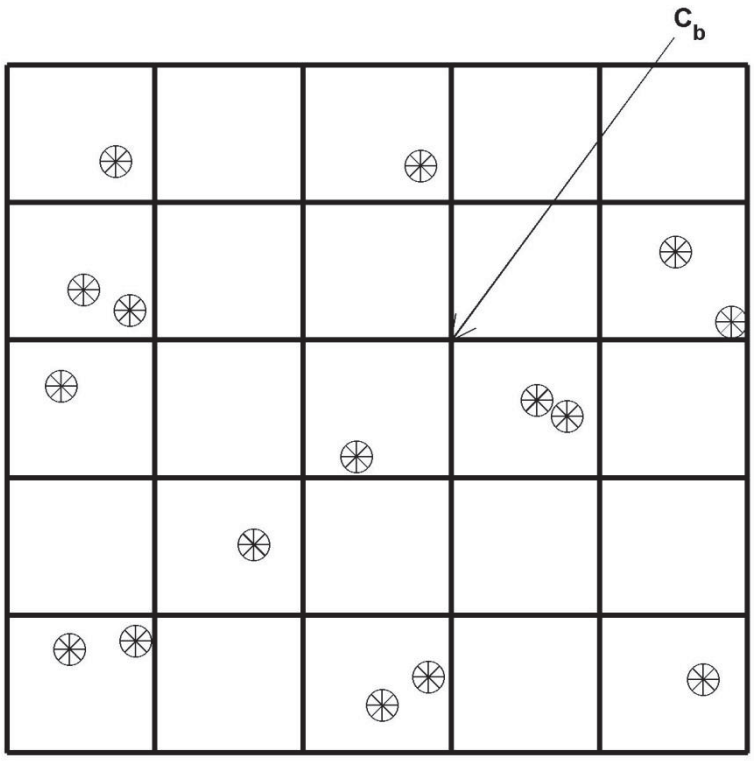

Fig. 1. Illustration of ocean data assimilation with $\boldsymbol{c}_b$ located at the grid points, and $\boldsymbol{c}_o$ located at the points '*". The ocean data assimilation is to convert the innovation, $\mathbf{d} = \boldsymbol{c}_o - \mathbf{H}\boldsymbol{c}_b$, from the observational points to the grid points.

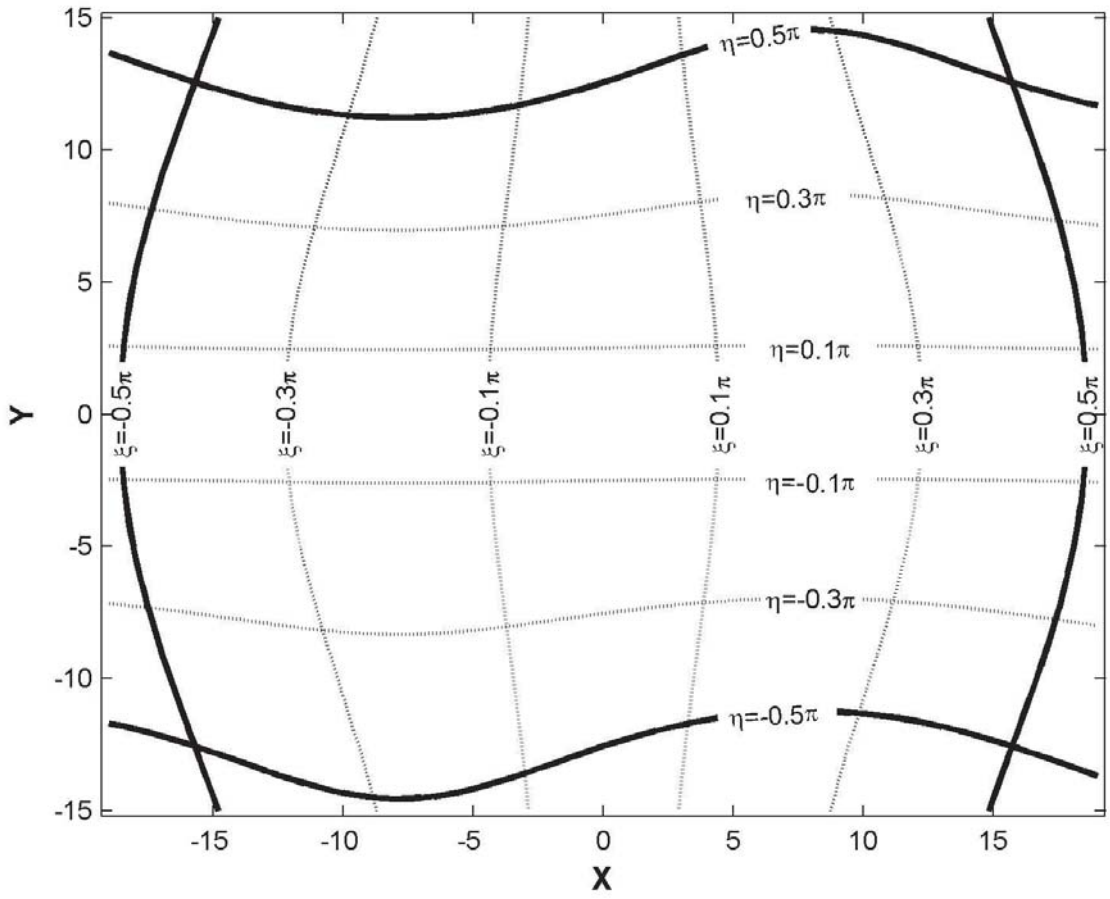

Fig. 2. Horizontal non-dimensional domain with four curved rigid boundaries with each boundary given by Eq. (32).

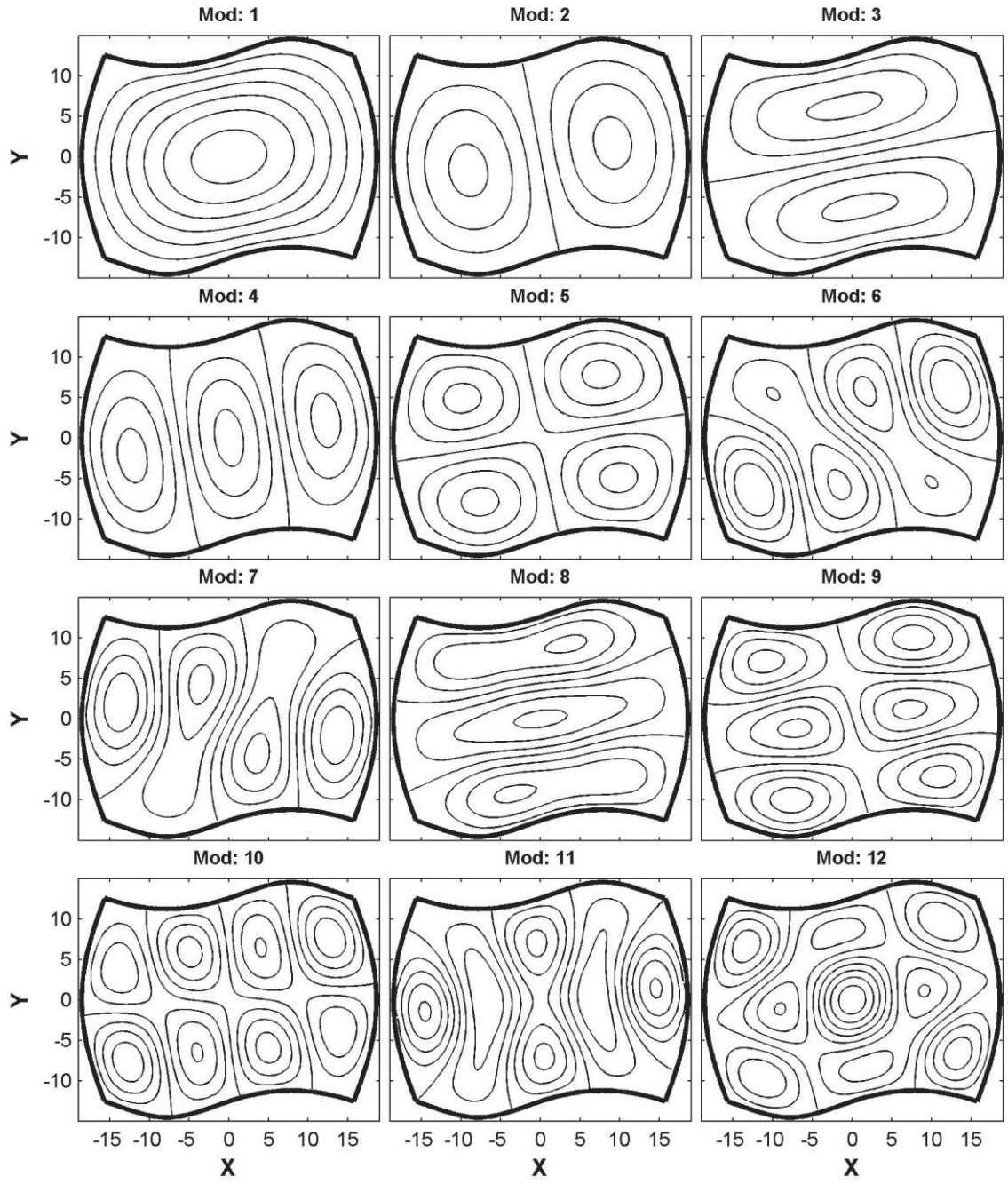

715
716
717 Fig. 3. Basis functions from ϕ_1 to ϕ_{12} for the domain depicted by Eq.(32).

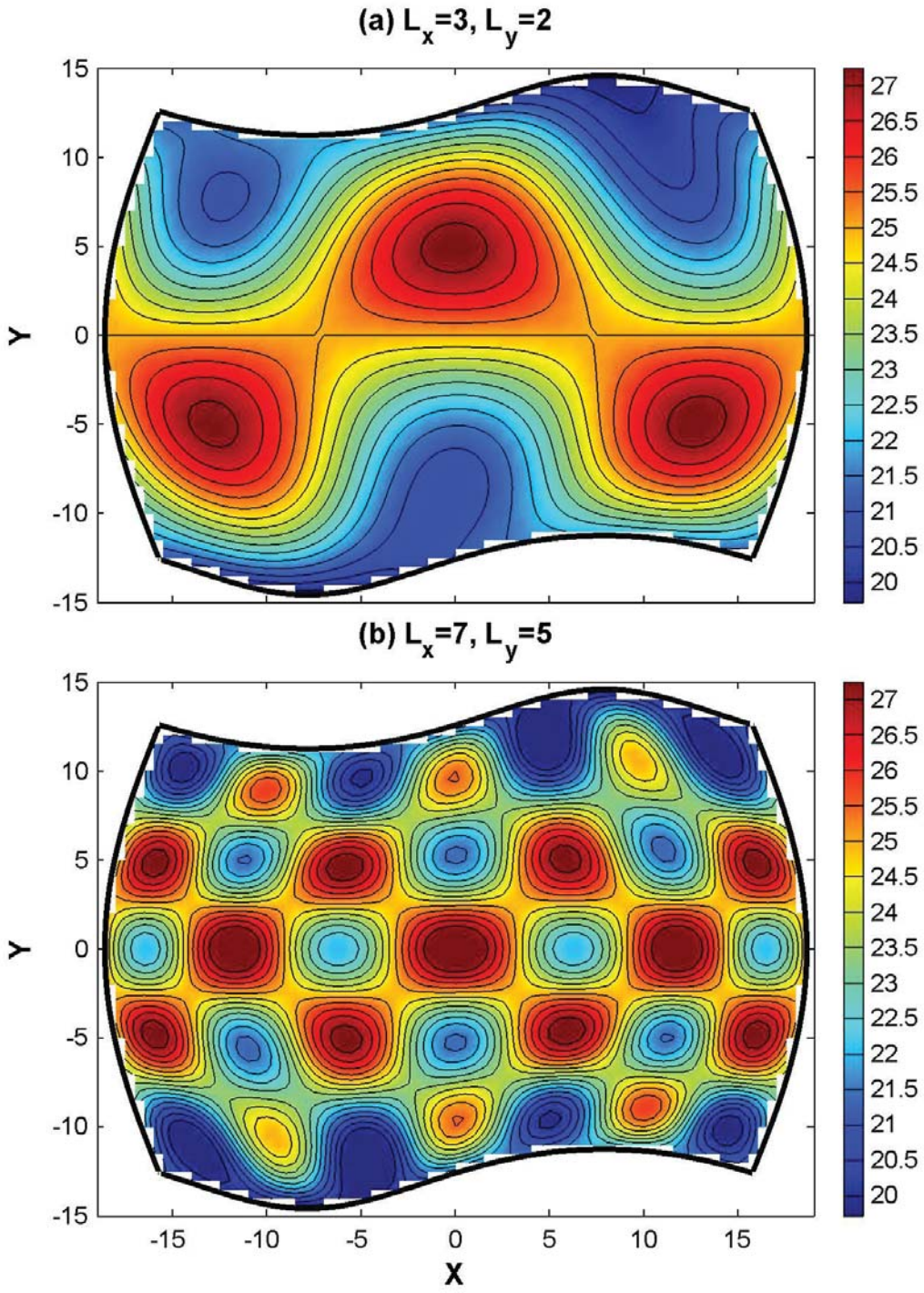

Fig. 4. "Truth" field c_t taken as (a) the analytical function (33) with large-scale eddy field L_x=3, L_y = 2, $\beta = \pi/2$, and (b) the analytical function (34) with small-scale eddy field L_x = 7, L_y = 5, β = 0.

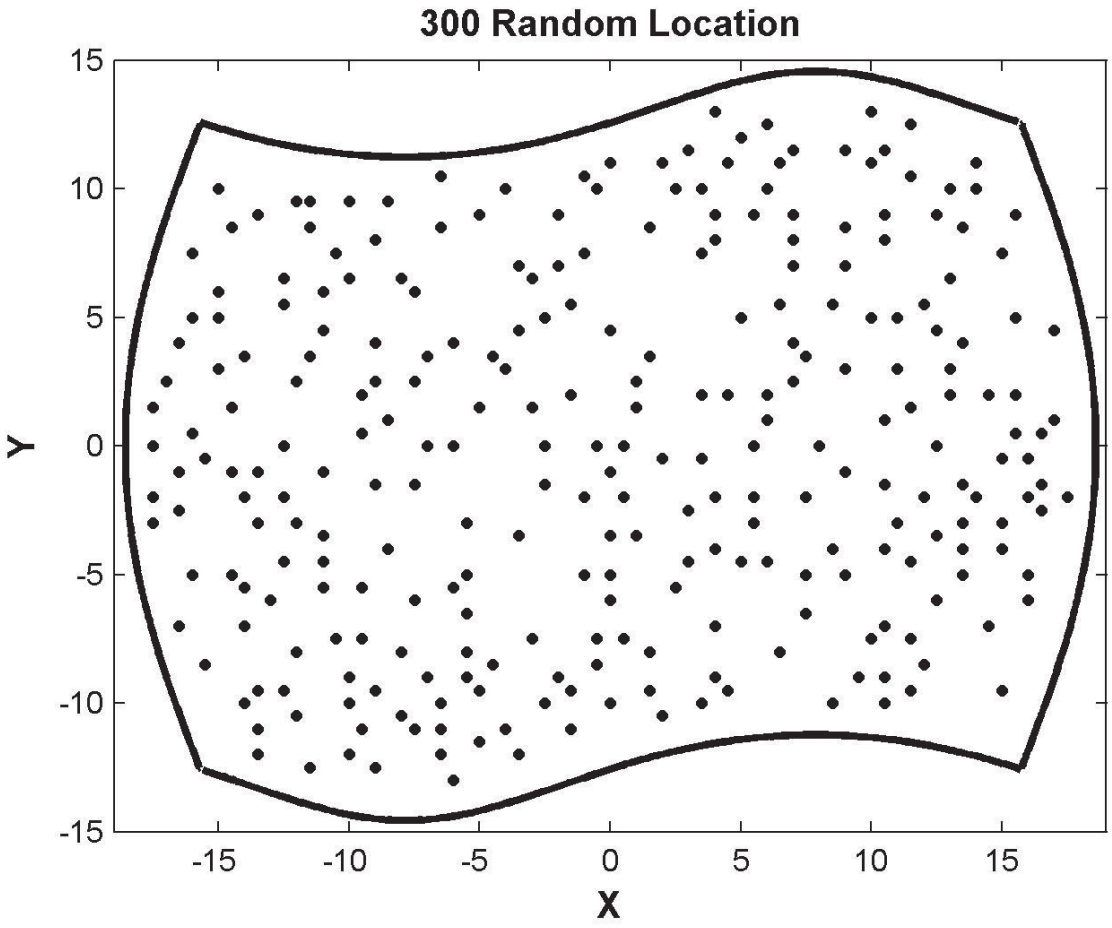

Fig. 5. Randomly selected locations (total: 300) inside the domain as “observational” points.

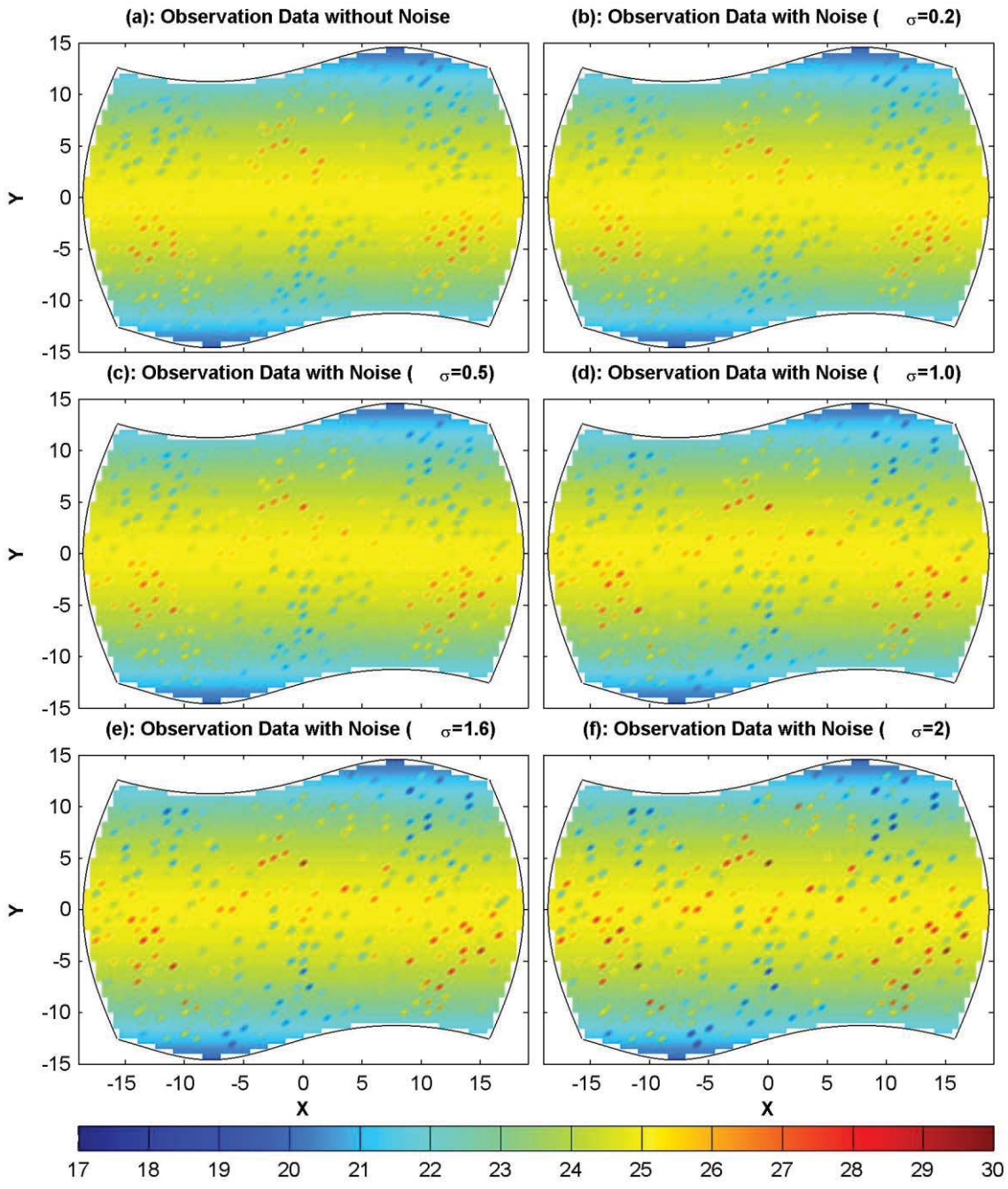

Fig. 6a. "Observational" data (c_o) from Fig. 4a with added white Gaussian noises of zero mean and various standard deviations: (a) 0 (i.e., no noise) (b) 0.2, (c) 0.5, (d) 1.0, (e) 1.6, and (f) 2.0.

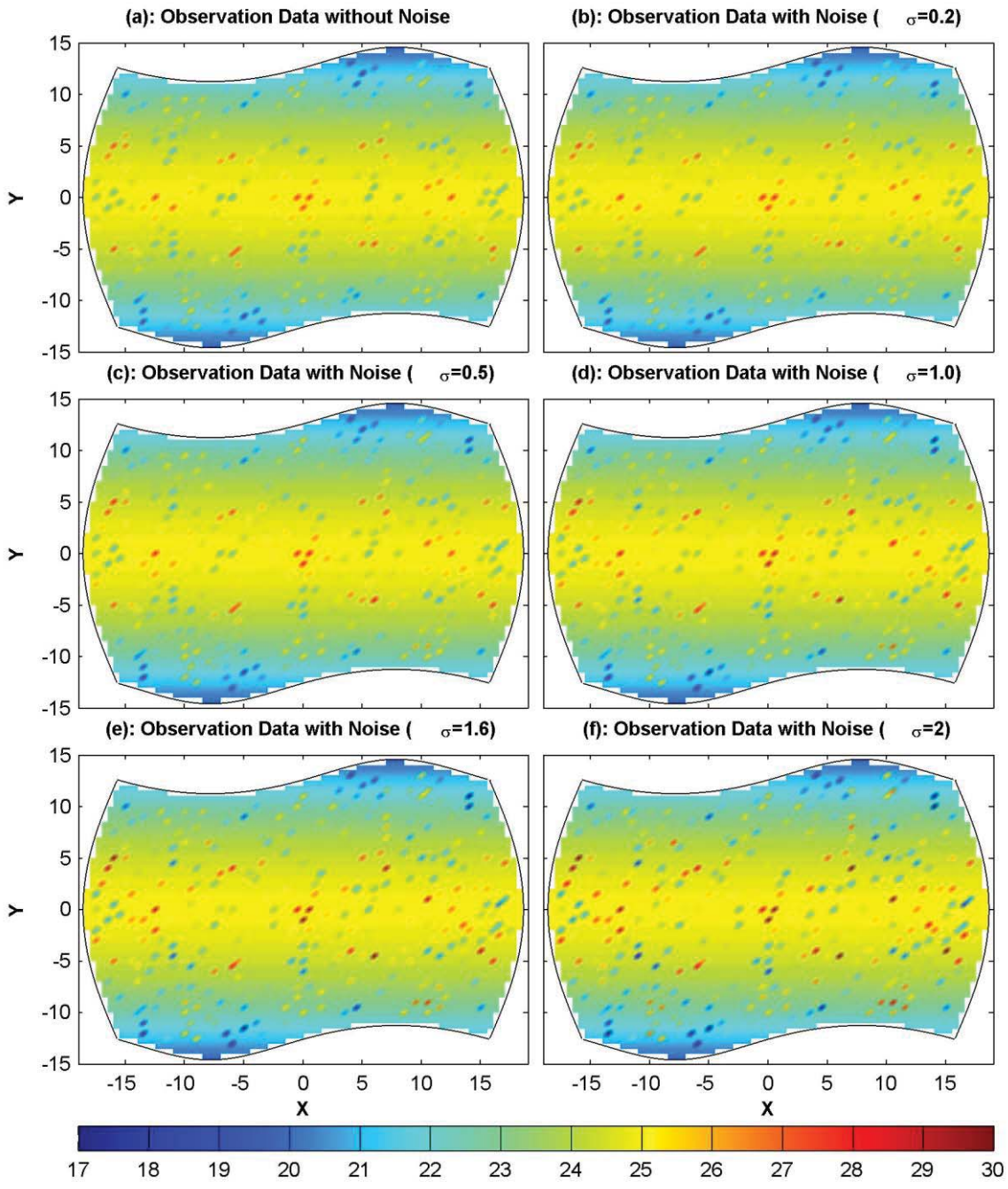

Fig. 6b. "Observational" data (c_o) from Fig. 4b with added white Gaussian noises of zero mean and various standard deviations: (a) 0 (i.e., no noise) (b) 0.2, (c) 0.5, (d) 1.0, (e) 1.6, and (f) 2.0.

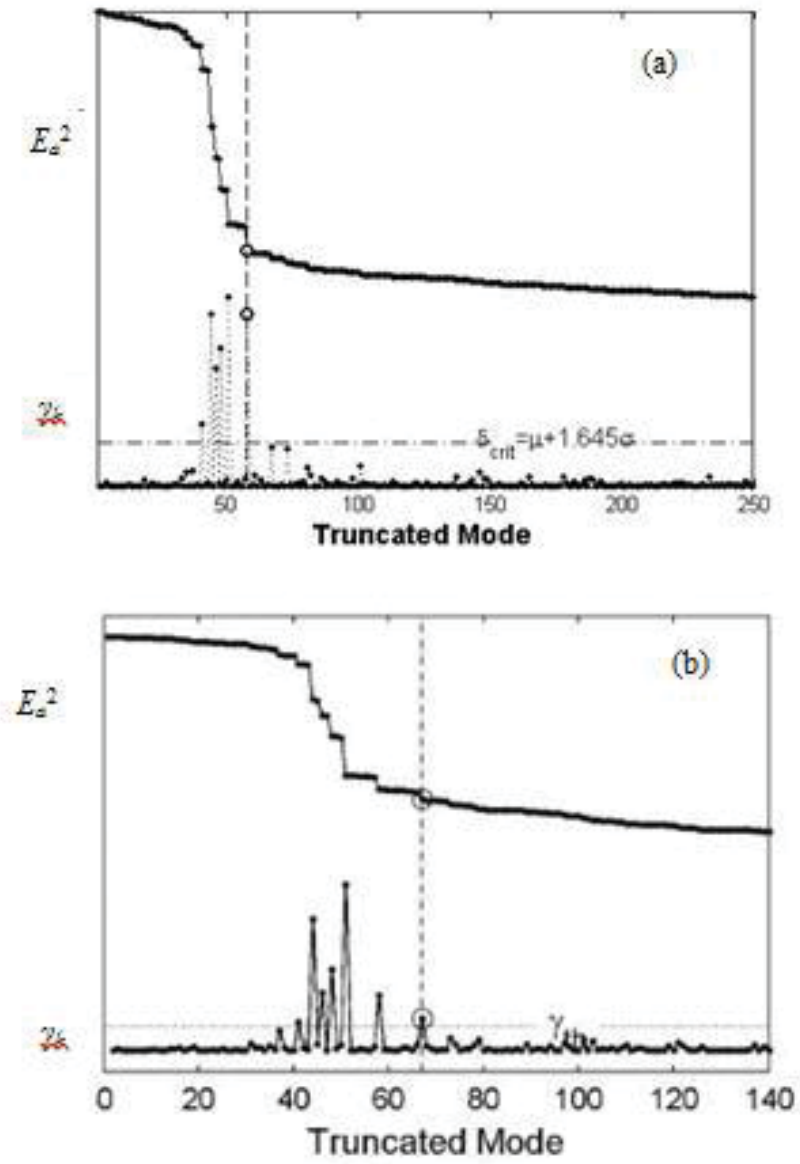

Fig. 7. Dependence of E_a^2 and γ_K on K for the "observational" data for the small-scale eddy field with $\sigma = 0.8$ and $e_o = 0.2$ at two significant levels of (a) $\alpha = 0.05$ ($z_{0.05} = 1.645$) and (b) $\alpha = 0.10$ ($z_{0.10} = 1.291$) as the threshold of mode truncation [see Eq.(27)]. The optimal mode truncation is 58 for $\alpha = 0.05$ and 67 for $\alpha = 0.10$.

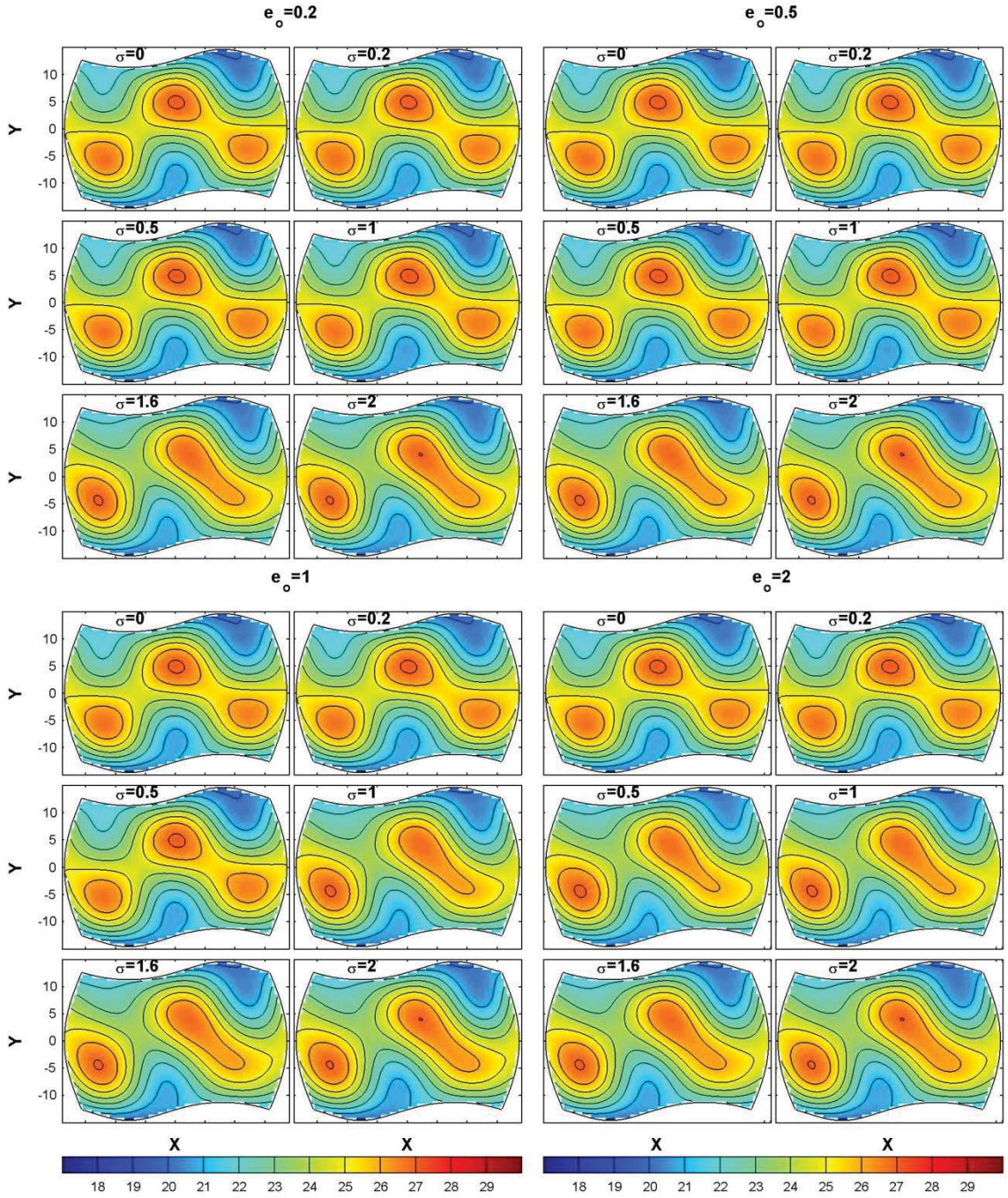

Fig. 8a. The analysis field c_a obtained by the spectral data assimilation [see Eq.(13)] using the steep-descending mode truncation with the significance level of $\alpha = 0.05$ from the "observations" shown in Fig. 6a with 6 noise (σ) levels (0, 0.2, 0.5, 1.0, 1.6, 2.0) and 4 values of e_o: (a) 0.2, (i.e., no noise), (b) 0.5, (c) 1.0, and (d) 2.0.

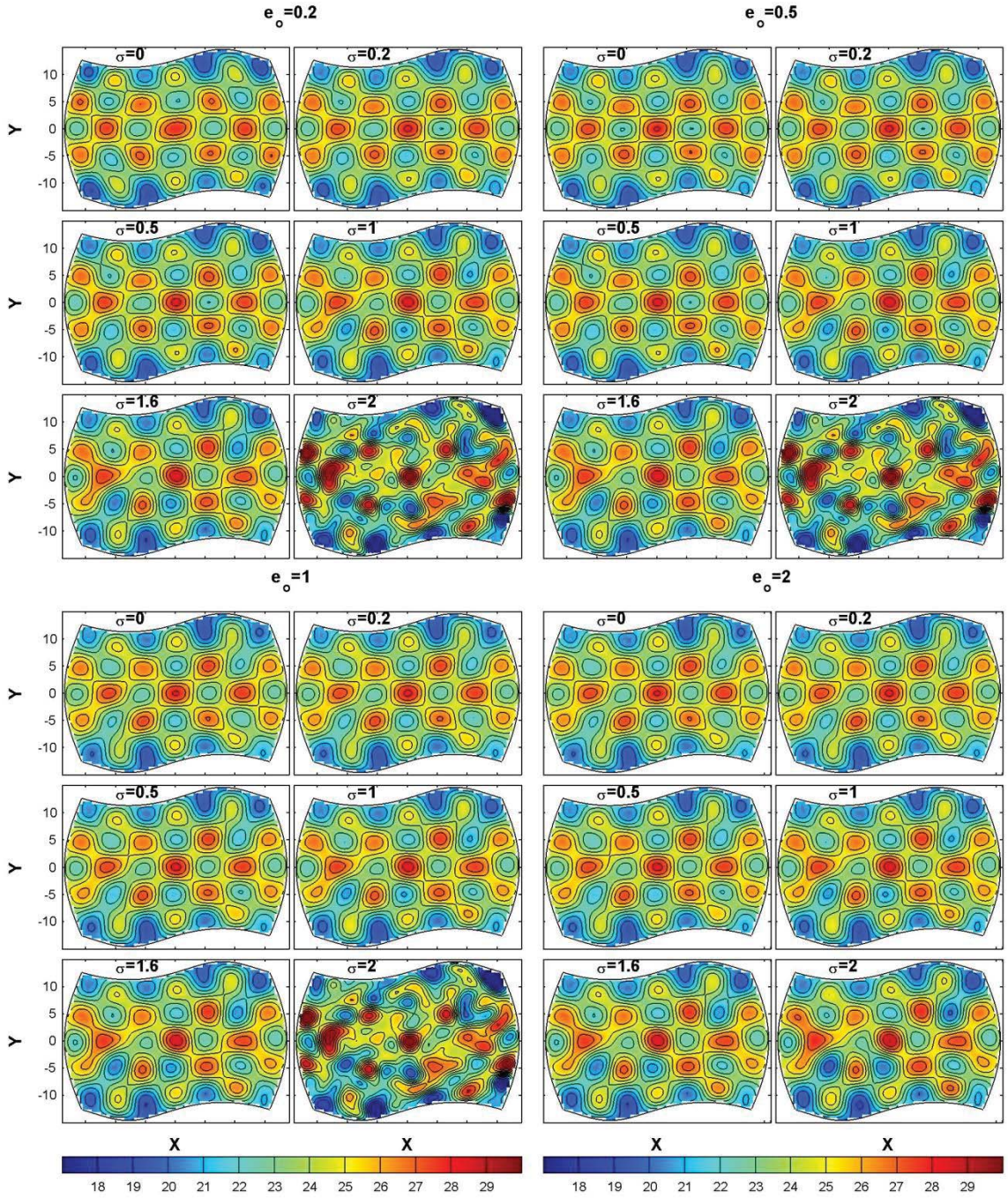

Fig. 8b. The analysis field c_a obtained by the spectral data assimilation [see Eq.(13)] using the steep-descending mode truncation with the significance level of $\alpha = 0.05$ from the "observations" shown in Fig. 6b with 6 noise (σ) levels (0, 0.2, 0.5, 1.0, 1.6, 2.0) and 4 values of e_o: (a) 0.2, (i.e., no noise), (b) 0.5, (c) 1.0, and (d) 2.0.

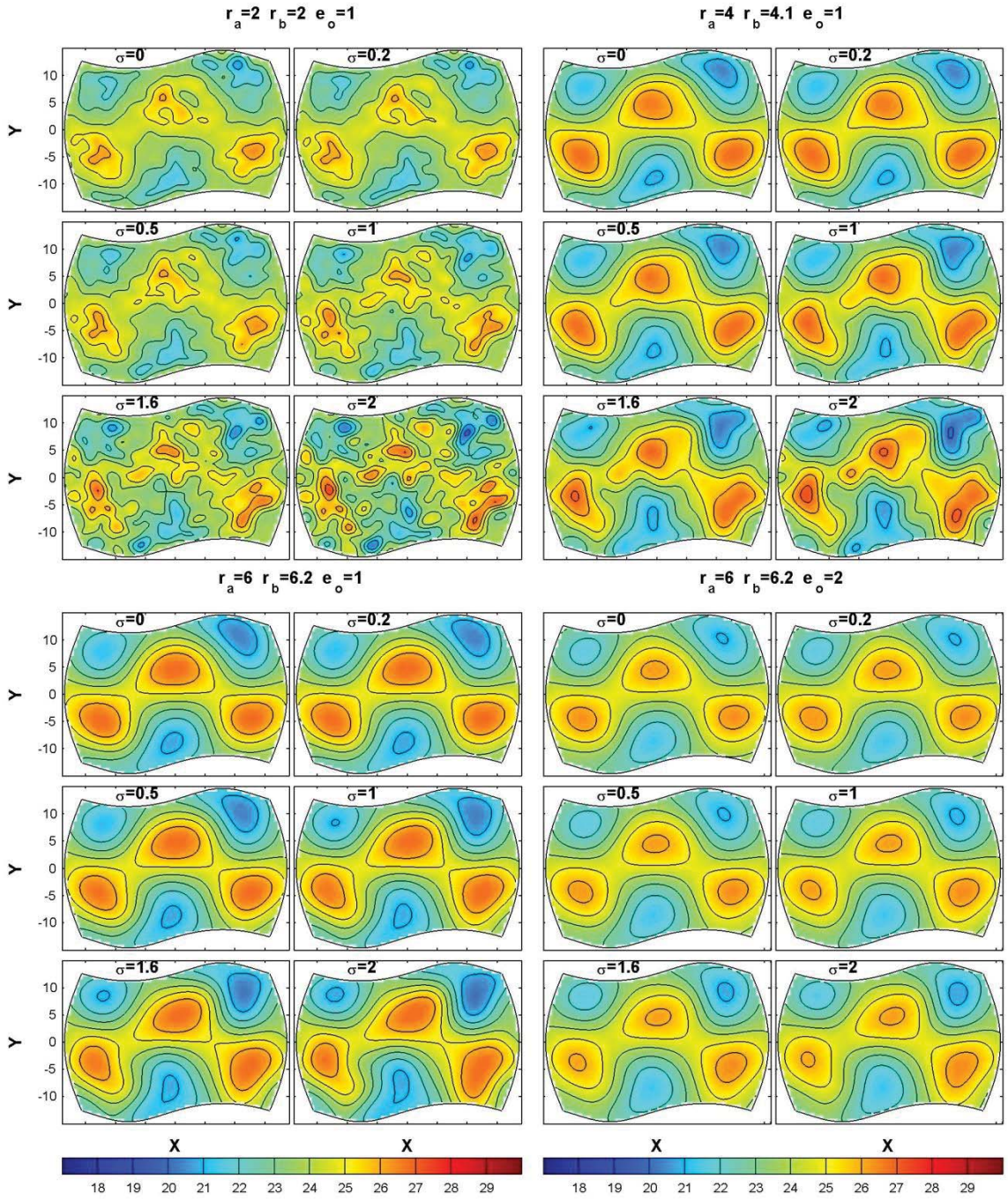

Fig. 9a. The analysis field c_a obtained by the OI data assimilation [see Eq.(9)] for "observations" shown in Fig. 6a various noise levels with various combinations of user-defined parameters (r_a, $r_{b,}$ e_o,): (2, 2.5, 1), (4, 5.5, 1), (6, 8.5, 1), and (6, 8.5, 2).

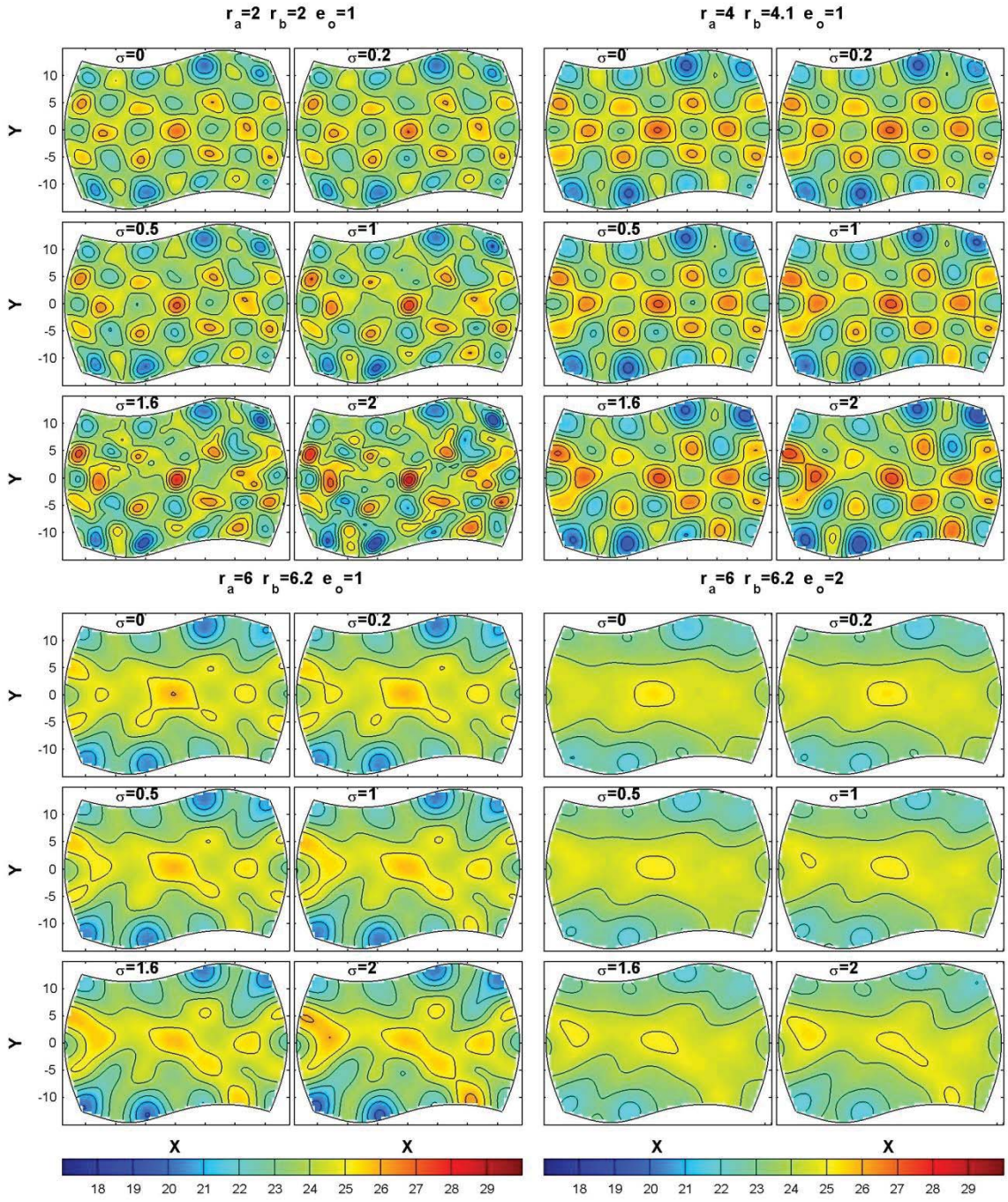

Fig. 9b. The analysis field c_a obtained by the OI data assimilation [see Eq.(9)] for "observations" shown in Fig. 6b various noise levels with various combinations of user-defined parameters (r_a, r_b, e_o,): (2, 2.5, 1), (4, 5.5, 1), (6, 8.5, 1), and (6, 8.5, 2).

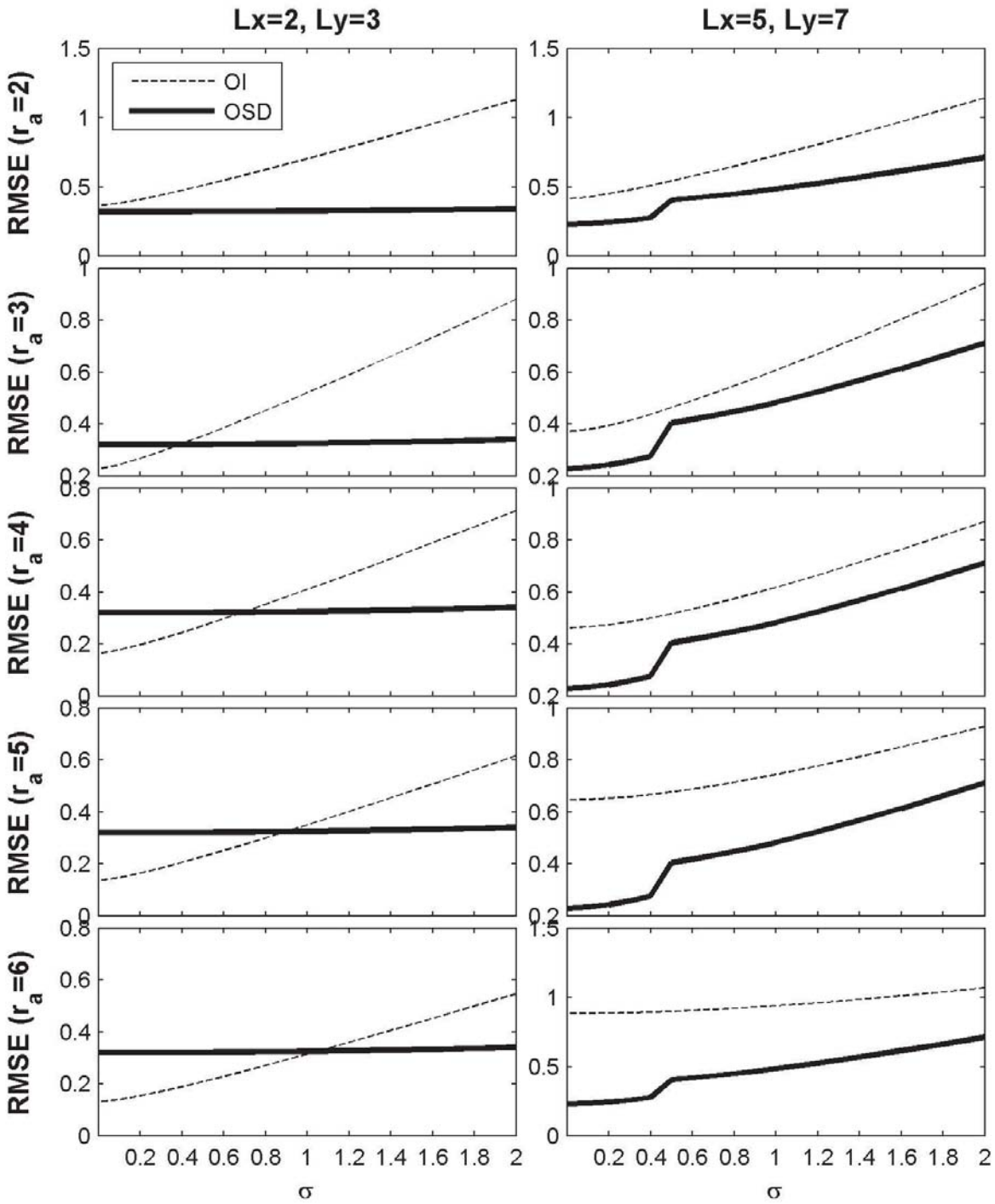

Fig. 10. Comparison between $R^{OI}(\sigma, r_a)$ and $\bar{R}^{OSD}(\sigma)$ of the analysis fields from the same "observations" with different noise levels with varying parameter r_a = (2, 3, 4, 5, 6) from top to bottom with the left panels using "observations" shown in Fig. 6a and the right panels using "observations" in Fig. 6b. The solid curves represent the OSD with the significance level of α = 0.05; and the dotted curves refer to the OI.

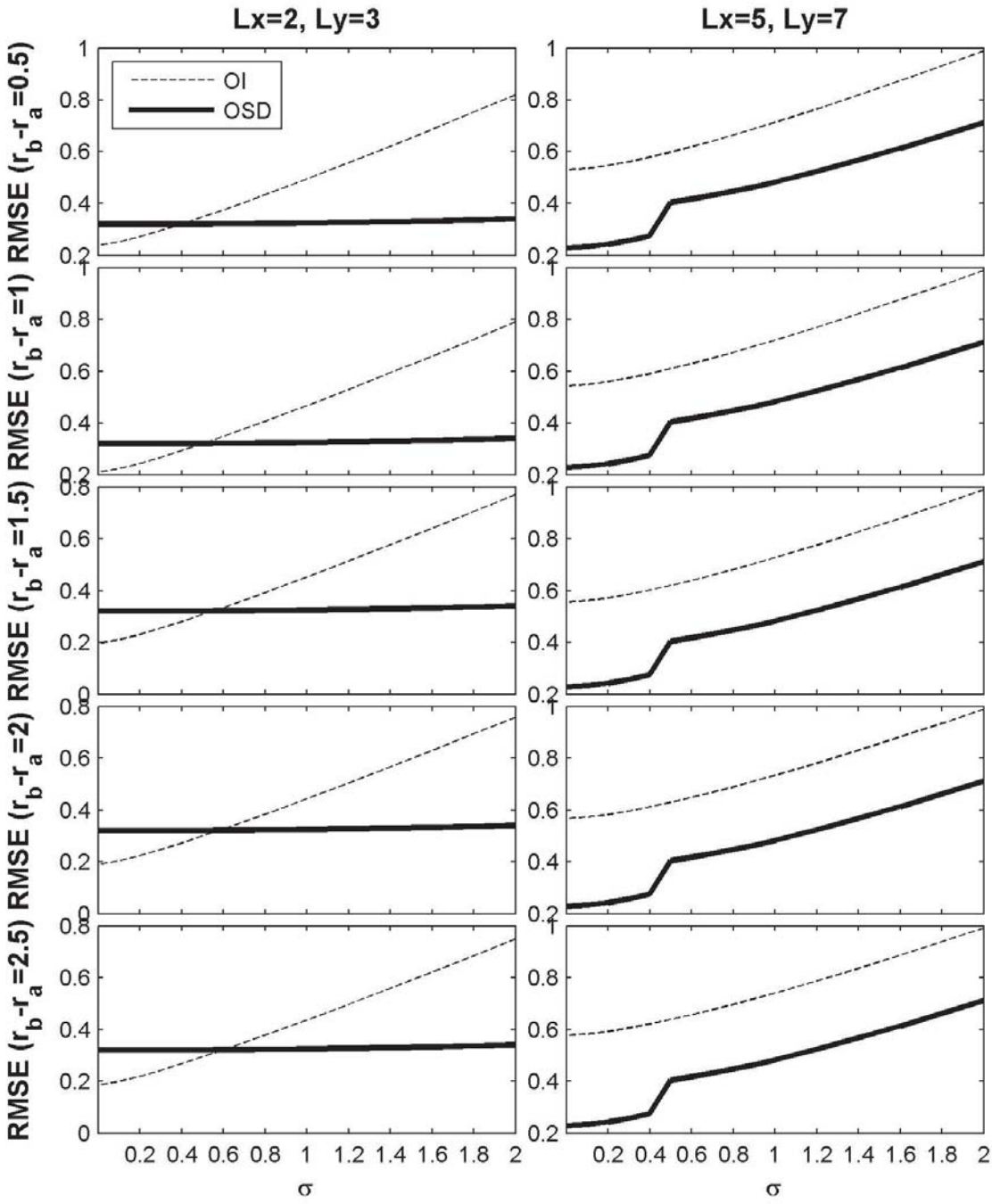

Fig. 11. Comparison between $R^{OI}(\sigma, r_b)$ and $\bar{R}^{OSD}(\sigma)$ of the analysis fields from the same "observations" with different noise levels with different $(r_b - r_a)$ = (0.5, 1.0, 1.5, 2.0, 2.5) with the left panels using "observations" shown in Fig. 6a and the right panels using "observations" in Fig. 6b. The solid curves represent the OSD with the significance level of α = 0.05; and the dotted curves refer to the OI.

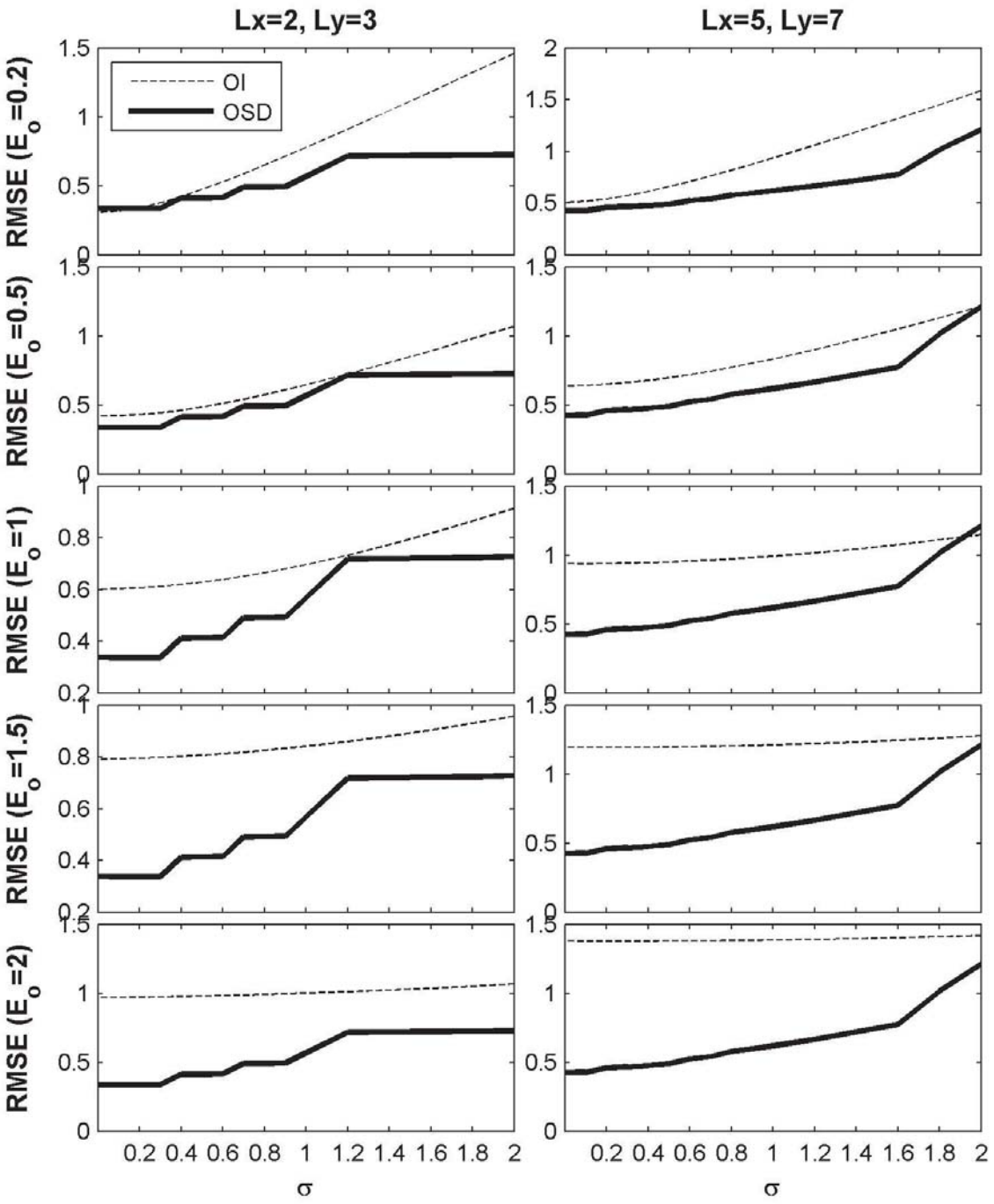

Fig. 12. Comparison between $R^{OI}(\sigma, e_o)$ and $R^{OSD}(\sigma, e_o)$ of the analysis fields from the same "observations" with different noise levels with varying parameter e_o = (0.2, 0.5, 1.0, 1.5, 2.0) from top to bottom with the left panels using "observations" shown in Fig. 6a and the right panels using "observations" in Fig. 6b. The solid curves represent the OSD with the significance level of α = 0.05; and the dotted curves refer to the OI.